

The Effects of the Uncertainty of Thermodynamic and Kinetic Properties on Nucleation and Evolution Kinetics of Cr-Rich Phase in Fe-Cr Alloys

by Mark Tschopp, Fei Gao, and Xin Sun

ARL-CR-0705

December 2012

Prepared for

U.S. Department of Energy
Nuclear Energy Advanced Modeling and Simulation Program
M3MS-12PN0606018

Under Contract
1120-1120-99

NOTICES

Disclaimers

The findings in this report are not to be construed as an official Department of the Army position unless so designated by other authorized documents.

Citation of manufacturer's or trade names does not constitute an official endorsement or approval of the use thereof.

Destroy this report when it is no longer needed. Do not return it to the originator.

Army Research Laboratory

Aberdeen Proving Ground, MD 2105

ARL-CR-0705

December 2012

The Effects of the Uncertainty of Thermodynamic and Kinetic Properties on Nucleation and Evolution Kinetics of Cr-Rich Phase in Fe-Cr Alloys

Mark Tschopp

Mississippi State University, Starkville, MS 39759, USA

Fei Gao and Xin Sun

Pacific Northwest National Laboratory (PNNL), Richland, WA 99352

Prepared for

U.S. Department of Energy

Nuclear Energy Advanced Modeling and Simulation Program

M3MS-12PN0606018

Under Contract

1120-1120-99

REPORT DOCUMENTATION PAGE			Form Approved OMB No. 0704-0188		
Public reporting burden for this collection of information is estimated to average 1 hour per response, including the time for reviewing instructions, searching existing data sources, gathering and maintaining the data needed, and completing and reviewing the collection information. Send comments regarding this burden estimate or any other aspect of this collection of information, including suggestions for reducing the burden, to Department of Defense, Washington Headquarters Services, Directorate for Information Operations and Reports (0704-0188), 1215 Jefferson Davis Highway, Suite 1204, Arlington, VA 22202-4302. Respondents should be aware that notwithstanding any other provision of law, no person shall be subject to any penalty for failing to comply with a collection of information if it does not display a currently valid OMB control number.					
PLEASE DO NOT RETURN YOUR FORM TO THE ABOVE ADDRESS.					
1. REPORT DATE (DD-MM-YYYY) December 2012		2. REPORT TYPE Final		3. DATES COVERED (From - To) August 2009 to September 2012	
4. TITLE AND SUBTITLE The Effects of the Uncertainty of Thermodynamic and Kinetic Properties on Nucleation and Evolution Kinetics of Cr-Rich Phase in Fe-Cr Alloys			5a. CONTRACT NUMBER 1120-1120-99		
			5b. GRANT NUMBER		
			5c. PROGRAM ELEMENT NUMBER		
6. AUTHOR(S) Mark Tschopp,* Fei Gao,** and Xin Sun**			5d. PROJECT NUMBER		
			5e. TASK NUMBER		
			5f. WORK UNIT NUMBER		
7. PERFORMING ORGANIZATION NAME(S) AND ADDRESS(ES) U.S. Army Research Laboratory ATTN: RDRL-WMM-F Aberdeen Proving Ground, MD 21005			8. PERFORMING ORGANIZATION REPORT NUMBER ARL-CR-0705		
9. SPONSORING/MONITORING AGENCY NAME(S) AND ADDRESS(ES) U.S. Department of Energy, NEAMS Program (through PNNL) 906 Battelle Blvd. Richland, WA 99352			10. SPONSOR/MONITOR'S ACRONYM(S)		
			11. SPONSOR/MONITOR'S REPORT NUMBER(S)		
12. DISTRIBUTION/AVAILABILITY STATEMENT Approved for public release; distribution unlimited.					
13. SUPPLEMENTARY NOTES *Mississippi State University, Starkville, MS 39759, USA; **Pacific Northwest National Laboratory (PNNL), Richland, WA 99352					
14. ABSTRACT The objective of this research is to develop a framework capable of exploring uncertainty quantification due to atomic-level simulations in iron-chromium (Fe-Cr) systems, particularly associated with defect segregation in grain boundaries (GBs). We have applied this approach to the interaction between point defects (vacancies and self-interstitial atoms [SIAs]) and elements with GBs in body-centered cubic (BCC) Fe, as an example, and then extended to Fe-helium (He) and Fe-Cr systems. The present results provide detailed information about the interaction energies of point defects and elements with symmetric tilt grain boundaries (STGBs) in Fe and the length scales involved with point defect absorption and element segregation to/by GBs. In one example, both low and high angle GBs were found to be effective sinks for point defects, with a few low- Σ GBs (e.g., the $\Sigma 3\{112$ twin boundary) that have properties different from the rest. Additionally, the effect of GB energy, disorientation angle, and Σ -designation on metrics proposed to evaluate the boundary sink strength was explored; the strongest correlation occurred between the GB energy and the mean point defect formation energies. The significance of this research is in its applicability to quantifying, with some confidence, grain boundary interactions with defects and elements at the nanoscale.					
15. SUBJECT TERMS Uncertainty quantification, kinetics, thermodynamics, Fe-Cr alloys					
16. SECURITY CLASSIFICATION OF:			17. LIMITATION OF ABSTRACT	18. NUMBER OF PAGES	19a. NAME OF RESPONSIBLE PERSON
a. REPORT	b. ABSTRACT	c. THIS PAGE			19b. TELEPHONE NUMBER (Include area code)
Unclassified	Unclassified	Unclassified	UU	52	Kris Darling 410-306-0862

Contents

List of Figures	iv
List of Tables	v
Acknowledgments	vii
1. Summary	1
2. Introduction	2
3. Simulation Methodology	5
4. Simulation Results	7
4.1 Generating a GB structure database	7
4.2 Influence of GB Atomic Structure on Point Defect Formation Energies.....	9
4.3 Influence of Macroscopic GB Character on Defect Formation Energies	13
4.4 Characterizing the GB Site Preference, Site Density, and Site Strength	16
4.5 Quantifying the Interaction Length Scale of GBs	21
4.6 Extension to Fe-He system.....	23
4.7 Extension to Fe-Cr system	26
4.8 Framework for Interatomic Potential Development with Uncertainty Quantification..	29
5. Summary	32
6. References	34
List of Symbols, Abbreviations, and Acronyms	40
Distribution List	41

List of Figures

Figure 1. STGB misorientation-energy relationship for the (a) $\langle 100 \rangle$ and (b) $\langle 110 \rangle$ tilt axes. The low Σ GBs ($\Sigma \leq 13$) in each system are identified. The strongest cusps are the $\Sigma 3(112)$, the $\Sigma 11(332)$, and the $\Sigma 5(310)$ boundaries. (c) $\langle 100 \rangle$ STGB structures with structural units outlined for the $\Sigma 17(410)$, $\Sigma 5(210)$, $\Sigma 29(730)$, $\Sigma 5(310)$, and $\Sigma 17(530)$ boundaries.	8
Figure 2. Vacancy and interstitial formation energies as a function of spatial position for three $\langle 100 \rangle$ STGBs: $\Sigma 5(210)$, $\Sigma 29(730)$, and $\Sigma 5(310)$ boundaries.	10
Figure 3. Vacancy and interstitial formation energies for two low angle boundaries in the $\langle 100 \rangle$ STGB system: the $\Sigma 41(910)$ and $\Sigma 85(760)$ GBs.	12
Figure 4. (a) Vacancy and (b) interstitial formation energies as a function of distance from the GB for all $\langle 100 \rangle$ STGBs.	13
Figure 5. (a, b) Vacancy and (c, d) interstitial formation energies as a function of the GB energy for $\langle 100 \rangle$, $\langle 110 \rangle$, and $\langle 111 \rangle$ STGBs.	15
Figure 6. GB site preference is shown by plotting the vacancy binding energy against the corresponding interstitial binding energy for each site in this study.	17
Figure 7. Histograms of the GB (a, b) site density and (c, d) site strength for (a, c) <i>vacancies</i> and (b, d) <i>interstitials</i>	19
Figure 8. Evolution of the vacancy and interstitial mean binding energies as a function of the distance from the GB center.	22
Figure 9. Evolution of the (a) vacancy and (b) interstitial mean binding energies as a function of the distance from the GB center.	23
Figure 10. Formation energies of (a) He in substitutional sites, (b) He in interstitial sites, and (c) He ₂ in interstitial sites as a function of spatial position for six $\langle 110 \rangle$ STGBs in order of increasing misorientation angle (left to right).	25
Figure 11. Formation energies for He ₂ in the interstitial sites as a function of distance from the GB for six $\langle 110 \rangle$ STGBs.	26
Figure 12. Formation energies of Cr ₂ V as a function of spatial position for six $\langle 110 \rangle$ STGBs in order of increasing misorientation angle (left to right).	28
Figure 13. Formation energies for Cr ₂ V as a function of distance from the GB for four $\langle 100 \rangle$ STGBs.	29
Figure 14. Schematic of the generalized framework for interatomic potential development showing the Global and Local Approach stages along with their individual steps.	30
Figure 15. (a) Nanoscale calculations (black dots) and analytical surfaces for single He formation energies in the LA Potential Space Sampling and LA Analytical Model Generation step. Accurate development of analytical relationships between parameters and properties are critical for probing the interatomic potential design space. (b) Interatomic potential design map for the Fe-He system.	32

List of Tables

Table 1. Summary of point defect statistics for low- Σ STGBs ($\Sigma \leq 13$).	20
Table 2. Summary of mean point defect statistics for general boundaries in different systems...	21

INTENTIONALLY LEFT BLANK.

Acknowledgments

This work was supported by the U. S. Department of Energy's Nuclear Energy Advanced Modeling and Simulation (NEAMS) Program at the Pacific Northwest National Laboratory, which is operated by Battelle for the U. S. Department of Energy under Contract No. DE-AC05-76RL01830.

INTENTIONALLY LEFT BLANK.

1. Summary

We have developed a *framework to address uncertainty quantification due to atomic-level simulations in iron-chromium (Fe-Cr) systems, particularly associated with defect segregation in grain boundaries (GBs)*. We have applied this approach to the interaction between point defects (vacancies and self-interstitial atoms [SIAs]) and elements with GBs in body-centered cubic (BCC) Fe, as an example, and then extended to Fe-helium (He) and Fe-Cr systems. Molecular statics simulations were used to generate a GB structure database that contained ~170 GBs with varying tilt and twist character. Then, formation and binding energies were calculated at all potential GB sites within 15 Angstroms of the boundary. The present results provide detailed information about the interaction energies of point defects and elements with symmetric tilt grain boundaries (STGBs) in Fe and the length scales involved with point defect absorption and element segregation to/by GBs. Both low and high angle GBs were effective sinks for point defects, with a few low- Σ GBs (e.g., the $\Sigma 3\{112$ twin boundary) that have properties different from the rest. The formation energies depend on both the local atomic structure and the distance from the boundary center. Additionally, the effect of GB energy, disorientation angle, and Σ -designation on metrics proposed to evaluate the boundary sink strength was explored; the strongest correlation occurred between the GB energy and the mean point defect formation energies. Based on binding energies, conclusions can be drawn about the energetic preference of certain types of point defects and types of element configurations with the GB region. The length scale of interaction of point defects and He and Cr segregation to GBs is also calculated. In point defects, for instance, this length scale is over a full lattice unit larger for SIAs than for vacancies (mean of 6–7 Angstroms versus 10–11 Angstroms for vacancies and interstitials, respectively). An interatomic potential design framework was developed to explore the uncertainty associated with the interatomic potential development process.

2. Introduction

Future design of nuclear materials requires structural materials that can withstand extreme environment conditions. Displacement cascades caused by neutrons create lattice point defects (vacancies and interstitials), which can have profound effects on the physical and mechanical properties of these alloys through the creation of defects, defect clusters, defect-impurity complexes, voids, and defect-solute clusters (1). The ability of materials to handle radiation damage is directly related to their ability to remove point defects through various microstructural sinks and mechanisms (2). Characterizing the mechanisms by which point defects are produced, diffuse, recombine, and are absorbed by sinks can help both our understanding of radiation damage and can help in quantifying the evolution of the underlying material microstructure. Since many structural materials are polycrystalline in nature, GB interactions with vacancies, interstitials, and elements play a vital role in the resulting properties of the polycrystalline material.

Quantifying how point defects and elements interact with defect sinks, such as GBs, is also important for understanding radiation-induced segregation of solute and impurity atoms in metals. This topic is of great importance for reactor performance, as radiation-induced segregation is one of many factors that contribute to irradiation-induced stress corrosion cracking. For instance, during radiation-induced segregation, the flux of solute and impurity elements is highly coupled with the flux of vacancy and interstitials. As vacancies and interstitials tend to diffuse and bind to microstructural sinks (e.g., GBs, free surfaces, defect clusters), solute and impurity atoms are spatially redistributed in the vicinity of these sinks. The net result is an accumulation or a depletion of elements at these defect sinks, which can have deleterious effects on polycrystal properties. There have been a number of experimental studies to characterize and understand the mechanisms of radiation-induced segregation in a number of irradiated metal systems (3–13) as well as computational models. Interestingly, these models have to consider both the evolution of defect and defect clusters as well as their destinations. Hence, understanding both the interaction of point defects with GBs and the GB sink strengths may be important for such models.

Point defect behavior and radiation-induced segregation can also be influenced by the GB character of individual GBs. GB character refers to the five degrees of freedom associated with the misorientation between the crystallographic orientations of the two adjoining grains. Hence, GB character encompasses not only the misorientation angle, but also the GB plane and information pertaining to GB type (e.g., tilt versus twist, symmetric versus asymmetric, low angle versus high angle, Σ value). Experiments have shown that certain coincidence GBs (e.g., $\Sigma 3$ and $\Sigma 9$) have sink strengths (pertaining to radiation-induced segregation) that deviate from

that in general high angle GBs (14). Moreover, other experiments have shown differences between GBs in their ability to annihilate point defects (15). These results present an interesting opportunity for designing radiation-tolerant materials, i.e., the GB character of polycrystalline materials can be engineered to enhance their beneficial effects while reducing their detrimental effects, as was first proposed by Watanabe (16). Recent advances in both experimentally measuring the GB character distribution (17–21) and applying GB engineering to various material systems (22) may allow for improved materials design of radiation-tolerant materials through thermo-mechanical processing. However, while experiments can readily supply information pertaining to changes in macroscopic properties due to GB engineering, it is difficult to experimentally understand the behavior of GB character for individual boundaries. Hence, nanoscale simulations that probe how GB character and local atomic structure impacts radiation processes can provide insight into how GB character affects the ability of polycrystalline metals to mitigate radiation.

Electronic structure calculations and atomistic simulations in bicrystalline and nanocrystalline structures have provided a fundamental understanding of nanoscale details regarding point defect behavior at GBs in polycrystalline materials (23–32) as well as interfaces in nano-layered metal composites (33–35). Previous work has used atomistic simulations to examine the interaction of point defect and point defect clusters with GBs in two-dimensional (2D) columnar and three-dimensional (3D) nanocrystalline metals. For example, Samaras and colleagues (24–27) have used molecular dynamics (MD) studies of nanocrystalline metals to show that GBs act as sinks for SIAs after nearby cascade events, which also leads to the formation of stacking fault tetrahedron in the grain interior for fcc Ni. Millett et al. (28, 29) used molecular dynamics simulations of 2D columnar nanocrystalline Mo to investigate the ability of GBs to act as both a sink for point defects and a source for vacancies at high homologous temperatures ($T > 0.75T_m$). While these studies are instrumental to understanding the operating mechanisms induced by radiation, these types of studies have numerous GBs with many confounding effects. For instance, nanocrystalline microstructures contain complex GBs with different tilt and twist misorientations, triple junctions, and a distribution of grain sizes. Hence, it is often difficult to ascertain the influence of GB character on the point defect-GB interaction.

On the other hand, bicrystalline simulations can also be used to explore the influence of individual GB structure on point defect behavior/properties using both *ab initio* and molecular dynamics simulations. *Ab initio* techniques have been used to explore properties for only a few low- Σ boundaries due to the high computational expense of accounting for the electronic structure. However, the relatively inexpensive cost of molecular dynamics simulations enables GB studies that have yet to be realized using *ab initio* simulations because of the large number of atoms required or the time scales required. For example, displacement cascade (or collision cascade) simulations are one example of a computationally intensive simulations that requires both a large number of atoms and a long time scale for motion of defect species after the initial

primary knock-on atom event. Perez-Perez and Smith (31, 32) used bicrystal MD simulations of a $\Sigma 17(530)$ GB to investigate the structural rearrangement and absorption of point defects following the cascade event. They found that there are preferential sites within the boundary where defects tended to localize and that 85% of defects within the boundary are within a few Angstroms of the GB center. More recently, Bai et al. (23) used MD simulations and temperature accelerated dynamics to show that GBs can act as an effective sink for vacancies and interstitials through various mechanisms in Cu. In one such mechanism, interstitials are loaded into the boundary, which then acts as a source, emitting interstitials to annihilate vacancies in the bulk. Moreover, there are many studies that have explored point defect energetics in a few (predominantly low- Σ) GBs. For example, Kwok, Ho, Yip, and colleagues (36–38) examined diffusion in an Fe $\Sigma 5$ GB by examining the mechanisms by which vacancies migrate at high temperatures. Also, Mishin and colleagues (39–41) investigated point defect properties of multiple low- Σ boundaries in Cu to understand GB diffusion at low and high temperatures. Recently, Demkowicz et al. (42) investigated the effectiveness of $\Sigma 3$ coherent twins to act as sinks for radiation-induced point defects in nanotwinned Cu. While these studies are instrumental to mechanisms and responses for several GBs, it would also be beneficial to use the relatively low cost of bicrystal MD simulations to sample a larger distribution of boundaries and therefore understand how GB character may impact the ability of GBs to act as sinks for point defects. Moreover, this kind of study can provide a natural bridge to higher scale models by exploring extreme value statistics and uncertainty associated with GB absorption of point defects and their associated binding energies.

Consequently, atomistic simulations that incorporate a large number of GBs can shed light on how GB character influences point defect-related properties in polycrystalline materials. While MD simulations are much less expensive than *ab initio* simulations, very few simulations consider a large number of GBs in their analysis of GB-related properties. However, it is well known that polycrystalline metals have a large range of GB types and high resolution transmission electron microscopy has shown large differences in GB structures (43–46). The exact nature of the atomic structure at the GB plays an important role in material properties (47, 48). Hence, typically, MD simulations that consider a wide range of GBs have focused on structure-energy relationships in face-centered cubic (FCC) metals (49–63). In their seminal work on GB structure, Sutton and Vitek (49–51) investigated the structural elements that comprised symmetric and asymmetric tilt grain boundaries (ATGBs), how to classify these structural units, and their relationship to properties, such as the GB energy. Wolf (56–59) has investigated how GB degrees of freedom (associated with the GB structure) correlates with GB energy for various GB systems in FCC metals. Holm et al. (60) calculated energies of 388 GBs in Al, Au, Cu, and Ni and observed that the GB energy scales with the shear modulus. Tschopp and McDowell (63–65) have studied how the faceted atomic structure of ATGB systems relates to GB energy and structural units in Al and Cu. How GB character affects other properties has also been investigated. Olmsted, Foiles, and Holm (66, 67) calculated 388 distinct GBs for Ni

and Al and analyzed metrics for describing GB energy as well as how GB character influences GB mobility. McDowell, Spearot, Tschopp, Tucker, and colleagues (61, 68–75) have investigated how GB structure influenced GB dislocation nucleation mechanisms. DeWald and Curtin (76–78) have shown assorted dislocation/GB reactions for dislocation transmission through a range of GB structures. Recently, Tschopp et al. (79) used 50 STGBs to show that interstitials have an energetic driving force to preferentially bind to GB sites over vacancies. With an emphasis for design of the next generation of radiation-tolerant materials, clearly a methodology that can analyze how point defect absorption is influenced by GB character would be valuable.

Therefore, in this work, the research objective is to systematically investigate the influence of GB character on the formation energetics and length scales of point defects and elements at GBs at 0 K. Molecular statics are used to investigate the static energetics; the effect of entropy will need to be incorporated later to fully capture the absorption behavior of point defects at high temperatures. Fe is chosen as an ideal BCC structural material for this study. While our earlier work examined only $\langle 100 \rangle$ STGBs (79), herein STGBs with $\langle 100 \rangle$, $\langle 110 \rangle$, and $\langle 111 \rangle$ tilt axes as well as twist and ATGBs are chosen to investigate the point defect and element formation energies as a function of location within/around the GB. The scope of this research is to investigate these trends for pristine, minimum energy GBs; higher energy GB structures were not examined herein. The simulation results show not only how local atomic structure and GB character affect the formation energetics of point defects, but also provide GB site metrics and necessary length scale parameters for incorporating GB structure into higher scale models.

3. Simulation Methodology

The methodology used to calculate the point defect energetics at the GB is similar to approaches used in previous studies (e.g., references 39 and 41). The methodology used to analyze the formation energies of point defects and elements is grouped into three primary steps: initialize, test, and analyze. First, in the initialization step, the GB structure database is generated. Second, during the test step, GBs are selected from this database and defects are iteratively added to GB sites to calculate their formation energies. Third, during the analyze step, the calculated database of properties are examined to determine the influence of important factors, such as local atomic structure, distance from the GB, and GB character (misorientation angle, Sigma value, etc.).

The GB structure database was generated using a parallel molecular dynamics code, Large-scale Atomic/Molecular Massively Parallel Simulator [LAMMPS] (80). The equilibrium 0 K structure and energy for each GB was calculated using a bicrystal computational cell with 3D periodic boundary conditions consisting of two grains (81). The minimum distance between the two periodic boundaries in each computational cell was 12 nm. As with previous work, multiple

initial configurations with different in-plane rigid body translations and an atom deletion criterion were used to access the minimum energy GB structures (e.g., see references 63, 64, and 66). The Polak-Ribiere nonlinear conjugate gradient algorithm was used for the energy minimization process, whereby the simulation cell was also allowed to expand normal to the GB plane (56). Hundreds to thousands of potential atomic structures were sampled to generate each minimum energy structure. Hence, Vitek and colleagues (52–55) have shown that each GB can be composed of a multiplicity of different atomic structures at the GB, which are related to the arrangement of GB dislocations and can ultimately result in different GB properties. In contrast to the aforementioned work, the concentration here was on the minimum energy boundary structure of a large number of boundaries as opposed to a range of atomic structures for a few boundaries. Therefore, a GB structure database with ~170 minimum energy GBs was generated to assess the influence of GB character on the binding energy of vacancies and interstitials. This database primarily contains $\langle 100 \rangle$, $\langle 110 \rangle$, and $\langle 111 \rangle$ STGBs along with some ATGBs and STGBs. For initial generation of the structures, the updated Mendeleev et al. (82) interatomic potential was used (83). The Mendeleev et al. Fe potential is based on the embedded atom method formulation (84, 85) and performs very well with respect to the Density Functional Theory (DFT) values pertinent to radiation damage studies (86).

After generating the GB database, the next step is to examine the formation energies of vacancies and SIAs for various GBs. As an initial example, consider the $\Sigma 5(210)$ STGB shown in figure 1 (c). First, the $\Sigma 5(210)$ GB structure is obtained from the GB structure database and all GB sites within 15 Angstroms are identified (47 sites). Then, one GB site is selected and a point defect is added by either removing the atom at that site (vacancy) or adding an additional atom at a nearby interstitial position (the SIA). For the interstitial atoms, the atom was added approximately 0.5 Angstroms along the GB period direction (perpendicular to the tilt direction in the GB plane). Next, the simulation cell is relaxed through a nonlinear conjugate gradient energy minimization process and the total energy with the point defect is obtained. For vacancies, the formation energy for a particular site α , E_{vf}^{α} , is calculated by,

$$E_{vf}^{\alpha} = E_{GB,v}^{\alpha} - E_{GB} + E_{coh}. \quad (1)$$

Here, E_{coh} is the cohesive energy/atom of a perfect BCC lattice, and $E_{GB,v}^{\alpha}$ and E_{GB} are the total energies of the simulation cell with and without the vacancy. On the other hand, for SIAs, the formation energy for a particular site, $E_{SIA,f}^{\alpha}$, is calculated by,

$$E_{SIA,f}^{\alpha} = E_{GB,SIA}^{\alpha} - E_{GB} - E_{coh}, \quad (2)$$

where $E_{GB,SIA}^{\alpha}$ is the total energy of the simulation cell with the SIA placed at site α . Once these two simulations have run and the formation energies have been calculated, then this procedure is repeated for the other GB sites (e.g., the other 46 sites for the $\Sigma 5(210)$ GB). After the formation energies for all GB sites have been calculated, then another GB structure is obtained from the GB structure database and the process is repeated until all GBs have been sampled. This process

provides a GB property database of formation energies of point defects over numerous GB structures.

The strength of each GB as a sink for point defects is of particular interest in the present study. In an attempt to quantify the GB sink strength, we examine several potential metrics for the distribution of point defect formation energies at each boundary. The first metric to be examined is the minimum formation energy or the extreme value of this distribution, which may be indicative of the strength of the boundary to absorb point defects. However, it should also be mentioned that this quantity will likely change as point defects are absorbed into the boundary, thereby locally altering the GB structure. So, while this extreme value of the formation energy distribution may be important as to the *potential* change in energy due to absorption of a point defect by a particular boundary site, the *mean* change in energy may also shed light onto the overall strength of each boundary. Therefore, the second metric to be examined is the mean point defect formation energy, which will be comparatively insensitive to absorption of multiple point defects, but will not capture the extreme values of the formation energy distribution. The two metrics will help facilitate comparisons in the “sink strength” of boundaries between different GB degrees of freedom and types (e.g., tilt versus twist, symmetric versus asymmetric, etc.).

In the first part of this report, we focus mainly on the $\langle 100 \rangle$, $\langle 110 \rangle$, and $\langle 111 \rangle$ STGB systems. In general, GBs in these systems are easier to obtain a global minimum energy structure than for asymmetric boundaries (61, 66, 87). While substantial care was taken to sample a wide range of configurations for each boundary, in some instances negative point defect formation energies indicate that a lower GB energy can be obtained through adding/removing an atom from the GB; subsequently, these boundaries were removed from analyses that considered the minimum formation energies. There are a total of 135 GBs that contained all positive formation energies (50 $\langle 100 \rangle$, 38 $\langle 110 \rangle$, and 25 $\langle 111 \rangle$ STGBs, 15 twist boundaries, and 7 ATGBs). In a later analysis of mean GB properties, additional boundaries are included to help illustrate trends (171 total). Moreover, the last section of the report covers extensions of the point defect work to investigating the interaction between He and Cr configurations with GB structure.

4. Simulation Results

4.1 Generating a GB structure database

Generating a database of various GBs that are encountered in polycrystalline materials is important for understanding the interaction between radiation-induced point defects, elements, and the interface structure. Figures 1(a) and 1(b) show the GB energy as a function of misorientation angle for the $\langle 100 \rangle$ and $\langle 110 \rangle$ STGBs, respectively. The low order coincident site lattice (CSL) systems (low Σ value, $\Sigma \leq 13$) are also shown for each of the STGB systems: the

$\Sigma 5$ and $\Sigma 13a$ GBs for the $\langle 100 \rangle$ STGBs and the $\Sigma 3$, $\Sigma 9$ and $\Sigma 11$ GBs for the $\langle 110 \rangle$ STGBs. For the $\langle 100 \rangle$ tilt axis, only minor cusps are observed in the energy relationship, most noticeably at the $\Sigma 5(310)$ STGB (990 mJ/m^2) in the $\langle 100 \rangle$ tilt system. However, for the $\langle 110 \rangle$ tilt axis, the GB energy varies strongly with misorientation angle. The two deep cusps are the $\Sigma 3(112)$ twin boundary (262 mJ/m^2) and the $\Sigma 11(332)$ STGB (1039 mJ/m^2). In addition to many high angle boundaries, several low angle boundaries ($\leq 15^\circ$) were also generated.

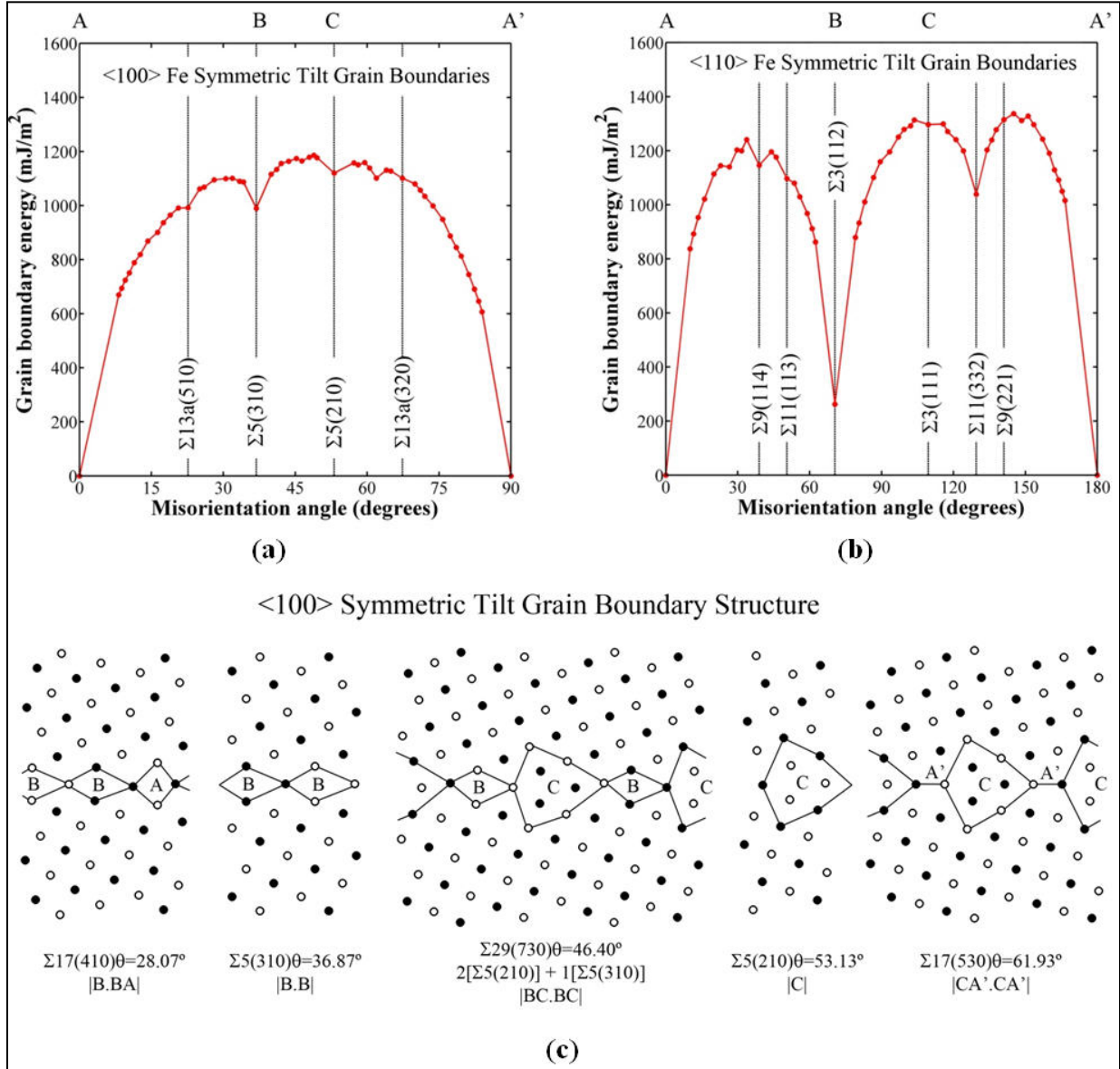


Figure 1. STGB misorientation-energy relationship for the (a) $\langle 100 \rangle$ and (b) $\langle 110 \rangle$ tilt axes. The low Σ GBs ($\Sigma \leq 13$) in each system are identified. The strongest cusps are the $\Sigma 3(112)$, the $\Sigma 11(332)$, and the $\Sigma 5(310)$ boundaries. (c) $\langle 100 \rangle$ STGB structures with structural units outlined for the $\Sigma 17(410)$, $\Sigma 5(210)$, $\Sigma 29(730)$, $\Sigma 5(310)$, and $\Sigma 17(530)$ boundaries.

Note: Regarding figure 1, black and white denote atoms on different {100} planes. The different structural units are labeled A, B, C, and A'. The $\Sigma 29(730)$ is composed of structural units from the two favored $\Sigma 5$ boundaries in a ratio determined by the structural unit model (Bishop, coincidence, 1968 [88]; Bishop, 1971, [89]; Sutton, 1983, [90]).

The GBs were specifically chosen to sample both low and high angle GB structures. For low angle boundaries, the GB is composed of an array of discrete dislocations and the corresponding energy can be calculated based on the classic dislocation model of Read and Shockley (91). For high angle boundaries, the spacing between lattice dislocations is small enough that dislocation cores overlap and the rearrangement of dislocation cores forms a local atomic structure within the GB (92). Sutton and Vitek analyzed the GB structure by characterizing the local atomic structure as structural units (49–51) and then the atomic structure of tilt GBs can be predicted using the structural unit model (51, 88, 89). The structural unit model works as follows. GBs with certain misorientation angles (and typically a low Σ value) can correspond to ‘favored’ structural units, while all other boundaries are characterized by structural units from the two neighboring favored boundaries. In general, this relationship holds for many pure tilt and twist boundary types with low index rotation axes. However, the structural unit model may not adequately describe the atomic structure in boundaries where dislocations readily dissociate (81, 87) or for mixed tilt-twist boundaries (90). Figure 1(c) shows an example for the $\langle 100 \rangle$ STGB system, where the two $\Sigma 5$ boundaries are favored STGBs and the $\Sigma 29(730)$ boundary is a combination of structural units from the two $\Sigma 5$ boundaries. The structural units for the $\Sigma 5(310)$ and $\Sigma 5(210)$ STGBs are labeled B and C, respectively. Also, notice that the ratio of structural units in the $\Sigma 29$ GB can be determined by the crystallographic relationship of the two favored boundaries, i.e., $\Sigma 29(730) = 2[\Sigma 5(210)] + 1[\Sigma 5(310)]$. In a similar manner, the two $\Sigma 17$ boundaries are combinations of the favored B and C structural units and “structural units” of the perfect lattice, A and A'. A similar relationship for GB structural units exists for the $\langle 110 \rangle$ STGB system as well, in that GBs at intermediate misorientation angles are composed of structural units of the adjacent favored boundaries. This example shows the structural units of the $\langle 110 \rangle$ tilt system, but each class of GBs (e.g., $\langle 100 \rangle$ tilt, $\langle 110 \rangle$ tilt, $\langle 111 \rangle$ tilt) in this report has its own favored boundaries and structural units. Additionally, the ratio and location of different structural units leads to different internal elastic strain fields within each boundary; therefore, the properties of GBs with intermediate misorientation angles is not easily determined through a linear relationship between the favored boundaries, as can be observed from the GB energy plots in figure 1 (a) and (b).

4.2 Influence of GB Atomic Structure on Point Defect Formation Energies

Examining how local atomic structure and GB sites contribute to the formation energy of point defects is important for understanding defect absorption behavior. Figure 2 shows the vacancy and interstitial formation energies that correspond to atomic positions in three $\langle 100 \rangle$ STGB structures shown in figure 1. In this plot, the relaxed point defect formation energies are shown in the unrelaxed atomic sites; realize that there is a 0.5 Angstroms shift between the unrelaxed

atomic sites for the interstitial atoms and vacancies, but we have shifted the unrelaxed interstitial atom sites by 0.5 Angstroms to coincide with the vacancy sites due to the GB periodicity. Note that in subsequent plots, we have used the unrelaxed atomic sites due to the difficulty of defining the relaxed vacancy location and to facilitate direct comparison between interstitial atoms and vacancies. The color bar in the upper (lower) set of images corresponds to GB sites with formation energies lower (higher) than in the bulk. The vacancy and SIA color bar is normalized by the corresponding formation energy in the bulk. In general, GB sites associated with atoms in the ‘B’ and ‘C’ structural units and nearby these structural units tend to have lower formation energies than in the bulk lattice (for both vacancies and SIAs). Moreover, since the color represents the fraction of the bulk formation energy, these contours show that the formation energies for interstitial atoms at the boundary have a much lower formation energy (relative to the bulk formation energy) than vacancies. So, while there is a similar formation energy for vacancies and interstitials (in agreement with previous simulations, e.g., references 39, 40, and 41), the fraction of the bulk formation energies is much lower for interstitials, which leads to higher binding energies to GBs. Subsequently, there is a corresponding larger energetic driving force for interstitials to segregate to the boundary in Fe over vacancies (79).

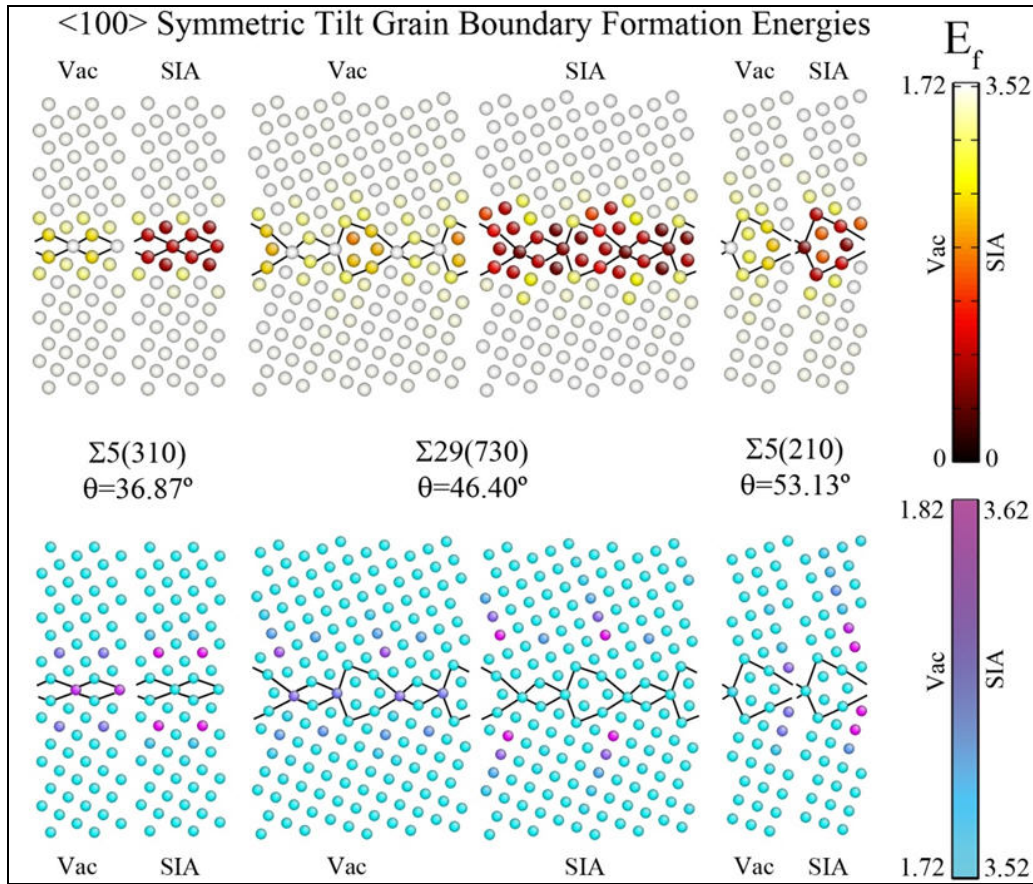


Figure 2. Vacancy and interstitial formation energies as a function of spatial position for three $\langle 100 \rangle$ STGBs: $\Sigma 5(210)$, $\Sigma 29(730)$, and $\Sigma 5(310)$ boundaries.

Note: In figure 2 the upper (lower) images show the distribution of formation energies lower (higher) than bulk values. The point defect formation energies are shown in the unrelaxed position; while the interstitial atoms are placed 0.5 Angstroms away from the vacancy sites, the atoms are shown in the same location due to the GB periodicity. The structural units are outlined and correspond to those shown in figure 1.

GB sites with a higher formation energy may also be important for understanding interfacial absorption of point defects. In figure 2, there are atoms lying at the intersection of structural units along the GB plane, which have a higher vacancy formation energy than the bulk, i.e., it is energetically more favorable for the vacancy to occupy a bulk lattice site. Interestingly, the corresponding sites for interstitial atoms do not have a higher formation energy, but rather a much lower formation energy. However, both vacancies and interstitials have some sites outside of the outlined structural units that also have higher formation energies than in the bulk lattice. These sites may be significant for defect absorption if they present an energy barrier for diffusion to the boundary or within the GB. However, in these cases and for the cases shown later, the magnitude of the formation energy increase is much smaller when compared to the magnitude of the potential formation energy decrease at numerous GB sites.

Low angle GBs also interact with point defects in the lattice. Figure 3 shows the vacancy and interstitial formation energies for two low angle GB structures ($\theta \leq 15^\circ$) in the $\langle 100 \rangle$ tilt system. The two boundaries are the $\Sigma 41(910)\theta=12.68^\circ$ low angle boundary and the $\Sigma 85(760)\theta=81.20^\circ$ low angle boundary ($\theta_{\text{eff}}=8.80^\circ$ when lattice symmetry is accounted for). The discrete dislocations that make up the GB structure are shown. Multiple low formation energy sites for both vacancies and interstitials surround the discrete dislocations that make up the low misorientation angle between the two grains. Again, compared to vacancies, the SIAs have much lower formation energies relative to formation energies in the bulk lattice. Interestingly, the dislocation type necessary for the $\Sigma 41(910)\theta=12.68^\circ$ and $\Sigma 85(760)\theta=81.20^\circ$ low angle boundaries impacts both the size and shape of the region with lower local formation energies for point defects. For instance, in the case of the $\Sigma 85(760)\theta=81.20^\circ$ low angle boundary, even atoms that are close to 8 Angstroms away still have a low vacancy formation energy. However, as the misorientation angle increases, the spacing between dislocations decreases and the affected regions begin to merge as the dislocation cores start to overlap. On the other hand, as the misorientation angle decreases, the low angle boundaries behave the same as isolated dislocations in a perfect lattice. Hence, low energy low angle boundaries will tend to have similar defect interaction properties as single dislocations within the lattice. Last, the lattice between the dislocations has formation energies comparable to the perfect single crystal, as would be expected.

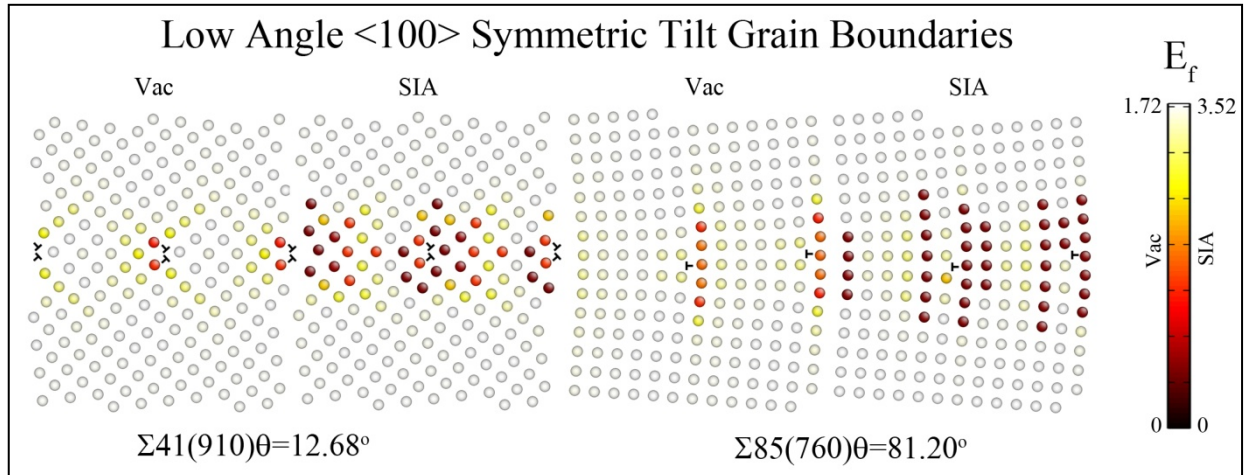


Figure 3. Vacancy and interstitial formation energies for two low angle boundaries in the $\langle 100 \rangle$ STGB system: the $\Sigma 41(910)\theta=12.68^\circ$ and $\Sigma 85(760)\theta=81.20^\circ$ GBs.

Note: Regarding figure 3, as in figure 2, the point defect formation energies are shown in the unrelaxed position with formation energies for interstitial atoms and vacancies shown in the same location due to periodicity. The affected region of lower defect formation energies surrounding the dislocations is noticeably larger for interstitials than for vacancies.

The vacancy and interstitial formation energies for each GB site as a function of position can provide insight into the length scale associated with point defect absorption by each boundary. Figure 4 (a) and (b) plot the vacancy and interstitial formation energies, respectively, as a function from distance from the GB for all 50 $\langle 100 \rangle$ STGBs. For this plot, all GBs were first centered such that the formation energies are symmetric about a value of 0 Angstroms for the GB distance. Then, a misorientation angle of 15° was used as a threshold for classifying boundaries as either low or high angle GBs. First, for vacancy formation energies in figure 4 (a), the majority of vacancy formation energies in the boundary have values that are much lower than the bulk values as well as a few energies that are slightly higher than bulk values. Second, the vacancy formation energies approach bulk values between 5–8 Angstroms away from the center of the GB. Third, for vacancy formation energies, the low angle boundaries tend to behave very similarly to high angle boundaries, aside from a few boundaries that show a band of lower formation energies associated with dislocations along the $\{110\}$ plane (inset image). Last, for vacancy formation energies, the data shows a symmetric relationship with both the minimum *and* maximum formation energies at a distance of ~ 0 Angstroms. So, while it is energetically favorable for vacancies to reside along the GB plane, possibly due to coincidence between the adjoining lattices, there are also energetically unfavorable sites along this plane as well (as shown in figure 2).

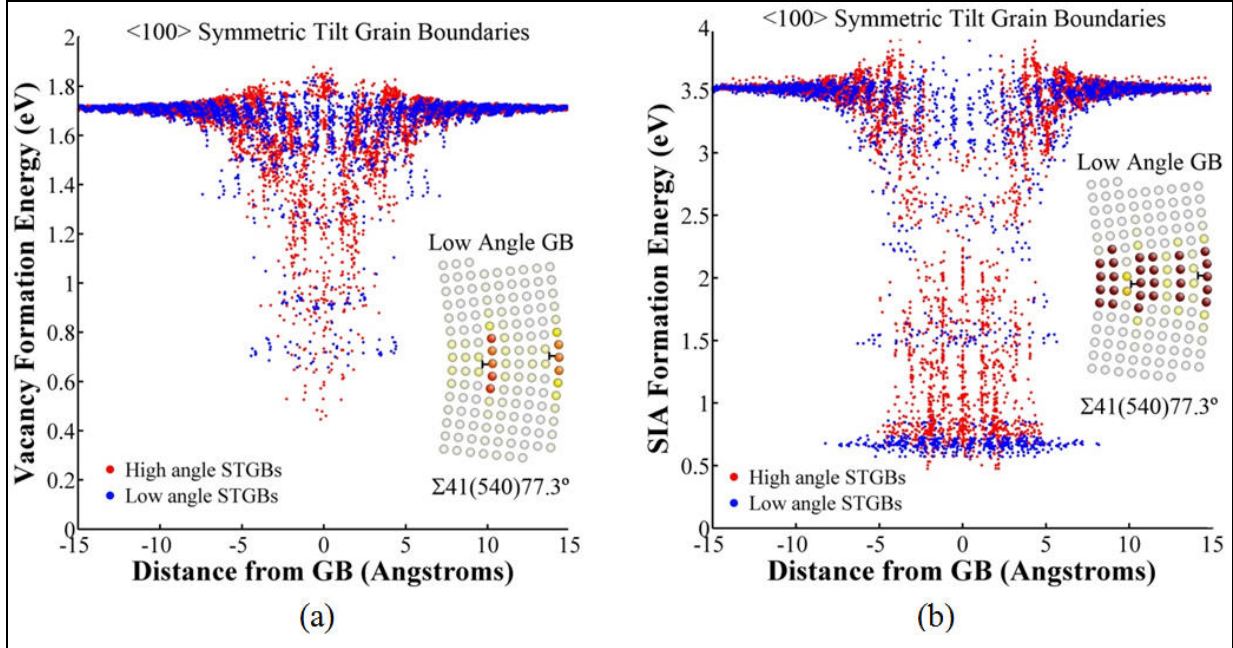


Figure 4. (a) Vacancy and (b) interstitial formation energies as a function of distance from the GB for all $\langle 100 \rangle$ STGBs.

Note: In figure 4 the vacancy and interstitial distances are the unrelaxed distances to facilitate comparison. The point defect formation energies are lower in the GB region, which extends ~ 5 Angstroms from the center of the boundary for the $\langle 100 \rangle$ tilt system.

For interstitial formation energies in the $\langle 100 \rangle$ tilt system (figure 4 [b]), there are some similarities with vacancies, but also some notable differences. First, there is a definitive contrast between low and high angle boundaries for interstitial formation energies. In the GB region (~ 5 – 8 Angstroms from center), the low angle boundaries tend to have either very low formation energies (discrete dislocation regions) or values comparable to bulk formation energies (intermediate single crystal regions). On the other hand, for high angle boundaries, the majority of interstitial formation energies are much lower than in the bulk lattice with very few points that are comparable to bulk lattice formation energies. Second, in the low angle boundaries, notice a much larger and more prominent clustering of low interstitial formation energies than those obtained for vacancy formation energies. Moreover, there is a much wider absorption length scale for interstitials in low angle GBs. Last, as opposed to figure 4 (a), the minimum formation energies are distributed throughout the GB (within ± 5 Angstroms of the GB center).

4.3 Influence of Macroscopic GB Character on Defect Formation Energies

During past few decades different modeling methods from atomistic, meso- and macro-scales, including the macroscopic GB character can also play a role in the absorption of point defects to the GB. To explore the influence of GB character on point defect absorption, we plotted (i) the distribution of defect formation energies (vacancies and interstitial atoms) and (ii) the mean

defect formation energies against several GB metrics: disorientation angle, GB energy, and the Σ value of the boundary. Here, the term disorientation angle is defined as the minimum misorientation angle when accounting for lattice symmetry. The Σ value represents the inverse fraction of coincident sites if the two adjoining lattices are viewed as interpenetrating and, in some cases, have been associated with properties that are different from general high angle GBs. Here we specifically focus on the correlation with GB energy; more information can be found in Tschopp et al. (93).

Figure 5 (a) and (b) show the vacancy and interstitial formation energy distributions as a function of the GB energy. The minimum formation energy is plotted as a larger symbol. The range of GB energies (600–1300 mJ/m²) is adequate to capture any general trends in the formation energy distributions. First, in figure 5 (a) and (b), the minimum formation energies for both vacancies and interstitials decrease with increasing GB energy. This trend is highly influenced by both the GB types and special boundaries. For instance, the $\langle 100 \rangle$ and $\langle 111 \rangle$ tilt systems have comparable formation energies, while the $\langle 110 \rangle$ tilt GB system has much lower minimum formation energies. In terms of GB energies, the distribution of GB energies in the $\langle 100 \rangle$ and $\langle 111 \rangle$ systems are lower than in the $\langle 110 \rangle$ system in terms of both mean and extreme values; hence, the trend is stronger, but is directly associated with the differences between GBs in different tilt systems. Moreover, this trend is influenced by the much higher vacancy and interstitial formation energies of the $\Sigma 3(112)$ STGB, a twin boundary that also has a very low energy. However, a low energy does not necessarily mean a higher formation energy for point defects. It is anticipated that low angle GBs (with much lower GB energies than those sampled here) in the $\langle 100 \rangle$, $\langle 110 \rangle$, and $\langle 111 \rangle$ tilt systems should have minimum formation energies similar to the low angle boundaries probed in this study.

Figure 5 (c) and (d) show the mean formation energy for vacancies and self-interstitial defects, respectively, within these GBs as a function of the GB energy. Additional symmetric/asymmetric tilt and twist GBs were added. There is an obvious trend with respect to the GB energy in these plots. The mean point defect formation energy decreases with increasing GB energy. Moreover, there is some uncertainty in the trend that can be associated with the differences in GB structures, i.e., the multiple potential structures for each GB energy associated with different GB systems or a multiplicity of GB structures can lead to different mean responses.

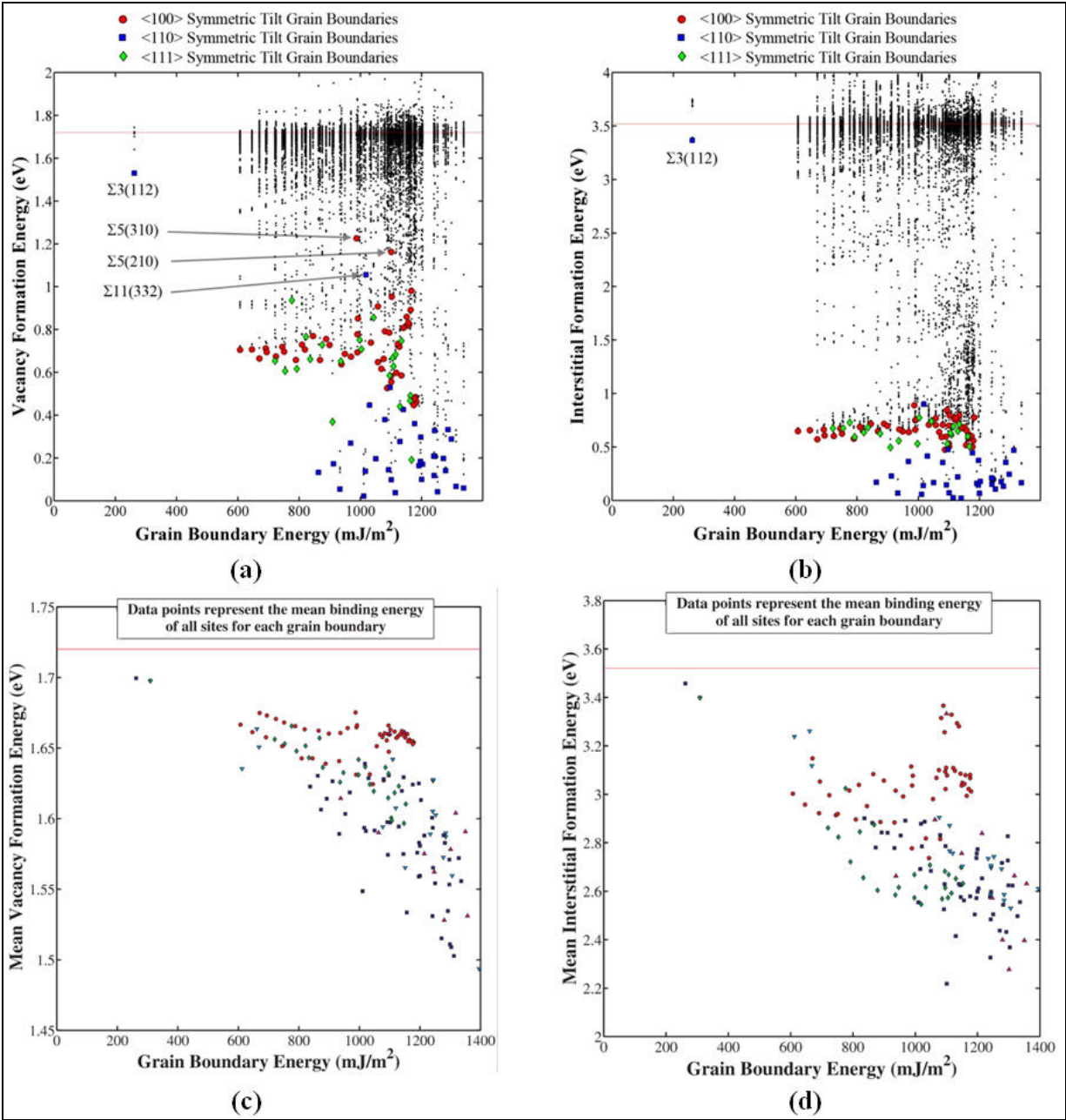


Figure 5. (a, b) Vacancy and (c, d) interstitial formation energies as a function of the GB energy for $\langle 100 \rangle$, $\langle 110 \rangle$, and $\langle 111 \rangle$ STGBs.

Note: In figure 5 the distribution of formation energies is plotted (black dots) as well as the minimum formation energy for each GB (symbol). (b, d) The mean formation energy for each GB is plotted against GB energy; additional twist and ATGBs are added to show the trend. The strongest trend occurs between the GB energy and the mean defect formation energies (c, d).

The current results present a slightly different picture than the work of Suzuki and Mishin (39) presented for a few Cu GBs. While the general trend is similar between the two works (i.e., minimum formation energy decreases with increasing GB energy), examining a large number of boundaries in the present work has shown that the GB tilt system plays an important role in the minimum formation energy as well. Moreover, Suzuki and Mishin (39) hypothesize that the minimum formation energy becomes negative at higher GB energies, indicating a maximum possible GB energy in STGBs in Cu. However, the trends within the GB tilt systems shown herein indicate that increasing the GB energy within a tilt system (e.g., $\langle 100 \rangle$ STGBs) does not necessarily trend towards more negative formation energies. What is most important is the initial structure of the GB, in particular whether the boundary is at a minimum energy structure or a near-minimum energy structure. For instance, negative formation energies are associated with GBs in a near-minimum energy structure where removing/adding an atom results in a slightly lower GB energy. This multiplicity of GB structures (52–55) is expected to play a prominent role in the minimum formation energies of point defects.

4.4 Characterizing the GB Site Preference, Site Density, and Site Strength

Further analysis of these simulations investigates both the GB site preference and methods for characterizing the GB sink strength for point defects in Fe. In doing this analysis, we will also analyze the “absorption” length scale associated with point defect absorption by GBs. The GB site preference can be evaluated by plotting the binding energy for vacancies and SIAs against each other for each GB site. This method has been previously applied to $\langle 100 \rangle$ STGBs (79). Figure 6 contains all the binding energies for the 135 minimum energy GBs (~75,000 simulations).

The GB binding energy at a particular site α is calculated by subtracting its formation energy from the bulk formation energy, $E_{binding}^{\alpha} = E_{f,bulk} - E_f^{\alpha}$. The line delineates sites where interstitial binding energy is greater than vacancy binding energies (above the line). The large amount of binding energies above this line indicates that the system energy is decreased more through interstitials occupying GB sites, rather than vacancies. Hence, this plot shows that there is an energetic driving force for interstitials to segregate to GB sites over vacancies. This finding suggests that GBs are, in fact, biased sinks for point defects based on the binding energy alone.

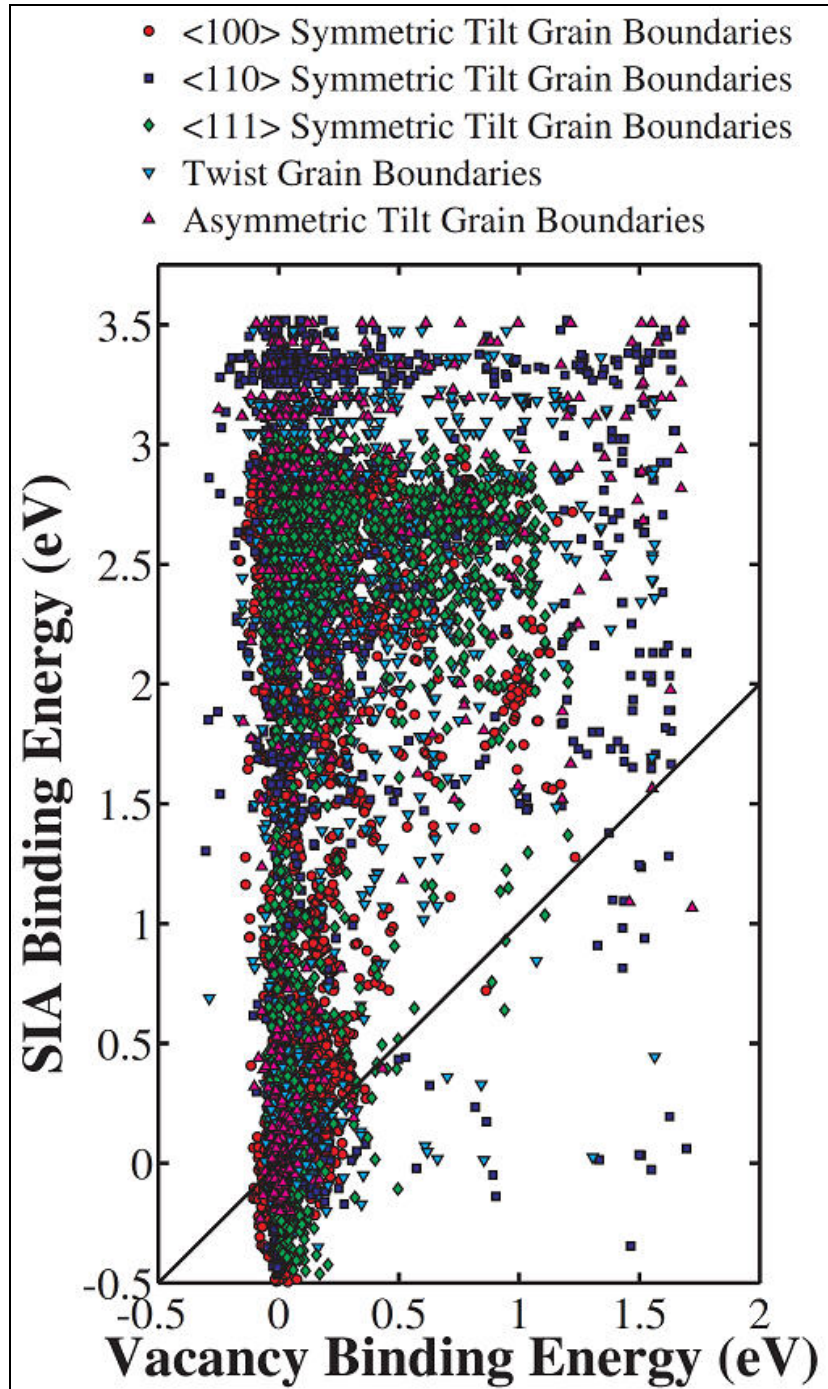


Figure 6. GB site preference is shown by plotting the vacancy binding energy against the corresponding interstitial binding energy for each site in this study.

Note: In figure 6 the line represents equal binding energies for vacancies and interstitial atoms. Similar to prior results in the $\langle 100 \rangle$ system (79, 93), albeit with a larger sampling of GBs, there is an energetic preference for binding of interstitials to GBs over vacancies.

Various figures of merit were defined to evaluate the interaction between GBs and point defects (vacancies and interstitial atoms). Figure 7 shows an example of some of these. In these histograms, a criterion is used to classify potential GB sites based on whether the binding energy for a particular site is greater than 0.05 electron volt (eV) (i.e., 0.05 eV lower formation energy than the bulk formation energy). Hence, this criterion eliminates the influence of atoms in the bulk lattice surrounding the boundary. The GB site density is then calculated by dividing the number of potential sites by the GB area. Figure 7 (a) and (b) show the resulting GB site density distributions for all GBs in this study. The associated mean, standard deviation, and maximum GB site density is also given in the histogram. The site density for SIAs is ~80% higher than for vacancies. Figure 7 (c) and (d) show the distributions of the GB site strength, as measured by the mean binding energy of all potential sites based on the same criterion. The mean binding energy for vacancies is 0.45 eV, while the mean binding energy for interstitials is 1.75 eV (~300% higher). Hence, both the number of GB sites and the mean GB site strength are much greater for interstitials than for vacancies. The breakdown of the various GB types is also displayed in this stacked histogram, showing the site density and site strength variability for each GB type. In general, the different GB types are dispersed over a wide range of site density and site strength values. In some cases, there are small differences between the GB systems. For example, in the GB site strength histograms, the $\langle 100 \rangle$ STGBs tend to have lower binding energies than the other GB systems. This data is also summarized in tables 1 and 2, which list the point defect data for individual low- Σ STGBs ($\Sigma \leq 13$) as well as the mean statistics for high- Σ STGBs ($\Sigma > 13$), twist boundaries, and ATGBs. The following study can provide guidance as to which GBs are different from or representative of more general high- Σ GBs.

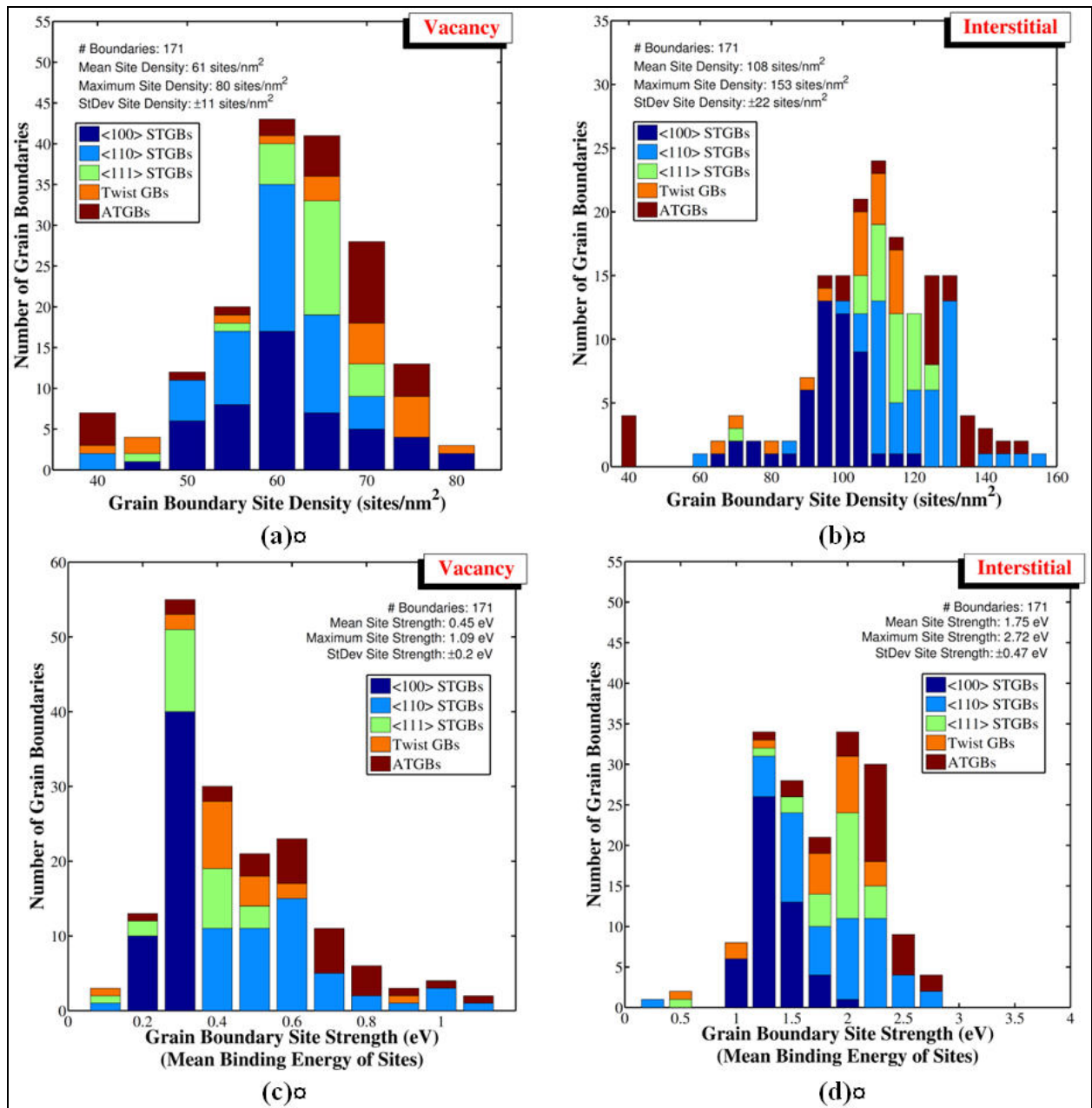


Figure 7. Histograms of the GB (a, b) site density and (c, d) site strength for (a, c) *vacancies* and (b, d) *interstitials*.

Note: In figure 7 the GB sites were classified according to a criterion that required the binding energy to be greater than 0.05 eV, distinguishing atoms in the bulk lattice from those in the GB.

Table 1. Summary of point defect statistics for low- Σ STGBs ($\Sigma \leq 13$).

Grain Boundary	γ_{GB} (mJ/m ²)	A_{GB} (nm ²)	Vacancy			Interstitial		
			ρ (site/nm ²)	$E_{f,min}$ (eV)	$E_{b,mean}$ (eV)	ρ (site/nm ²)	$E_{f,min}$ (eV)	$E_{b,mean}$ (eV)
			$\Sigma 3\{112\}\langle 110 \rangle \theta = 60.00^\circ$	262	0.20	40	1.53	0.13
$\Sigma 3\{111\}\langle 110 \rangle \theta = 60.00^\circ$	1297	0.28	42	0.29	1.03	149	-0.08	1.34
$\Sigma 3\{011\}\langle 111 \rangle \theta = 60.00^\circ$	309	0.35	46	1.44	0.13	69	2.94	0.45
$\Sigma 5\{012\}\langle 100 \rangle \theta = 36.87^\circ$	1096	0.18	60	1.23	0.26	88	0.75	1.29
$\Sigma 5\{013\}\langle 100 \rangle \theta = 36.87^\circ$	987	0.26	47	1.23	0.27	70	0.90	1.52
$\Sigma 7\{123\}\langle 111 \rangle \theta = 21.79^\circ$	1047	0.92	59	0.65	0.44	116	0.90	1.86
$\Sigma 9\{114\}\langle 110 \rangle \theta = 38.94^\circ$	1146	0.35	52	0.69	0.46	104	0.73	2.31
$\Sigma 9\{221\}\langle 110 \rangle \theta = 38.94^\circ$	1282	0.49	65	0.33	0.55	106	0.38	2.37
$\Sigma 11\{332\}\langle 110 \rangle \theta = 50.48^\circ$	1018	0.38	52	1.06	0.42	84	0.89	1.97
$\Sigma 11\{113\}\langle 110 \rangle \theta = 50.48^\circ$	1097	0.54	59	0.53	0.41	100	0.48	1.88
$\Sigma 13a\{023\}\langle 100 \rangle \theta = 22.62^\circ$	1094	0.29	68	0.80	0.24	95	0.76	1.08
$\Sigma 13a\{015\}\langle 100 \rangle \theta = 22.62^\circ$	992	0.42	58	0.86	0.26	96	0.77	1.20
$\Sigma 13b\{134\}\langle 111 \rangle \theta = 32.20^\circ$	1107	1.25	58	0.67	0.55	109	1.07	2.04

Table 2. Summary of mean point defect statistics for general boundaries in different systems.

Grain Boundary	γ_{GB} (mJ/m ²)	A_{GB} (nm ²)	Vacancy			Interstitial		
			ρ (site/nm ²)	$E_{f,min}$ (eV)	$E_{b,mean}$ (eV)	ρ (site/nm ²)	$E_{f,min}$ (eV)	$E_{b,mean}$ (eV)
$\langle 100 \rangle$ STGBs $\Sigma > 13$	988	0.83	62	0.72	0.27	96	0.68	1.36
$\langle 110 \rangle$ STGBs $\Sigma > 13$	1136	1.02	60	0.19	0.60	122	-0.15	1.91
$\langle 111 \rangle$ STGBs $\Sigma > 13$	974	1.62	64	0.69	0.35	115	0.69	1.92
All Twist GBs	1083	2.15	65	0.48	0.44	102	0.64	1.73
All ATGBs	1477	8.37	59	-1.05	0.63	109	-1.59	2.17

4.5 Quantifying the Interaction Length Scale of GBs

There is an inherent length scale associated with point defect absorption to GBs that is influenced by both the defect type and the GB character. In addition to the energetics, the length scales associated with the GB interface are also important for higher scale models that may require details of the sharp or diffuse nature of GBs and their interaction with point defects. Figure 8 shows how the mean vacancy and interstitial binding energies decrease as a function of distance from the boundary. For this plot, the binding energies are calculated using bins that are 2 Angstroms wide. As shown in the inset histogram, the mean binding energy for each boundary is calculated for each bin. The plotted mean binding energy for each bin is calculated by taking the mean of the corresponding histogram; this process guarantees that each boundary is equally weighted. The error bars are equal to one standard deviation from the mean vacancy and interstitial binding energies for each bin. This plot shows that the interstitial binding energies are much greater than vacancy binding energies, similar to previous results. The mean binding energy tends to be greatest near the GB center and decreases as the distance from the GB center increases. Moreover, the mean vacancy binding energy approaches 0 eV at 6–7 Angstroms, whereas the mean interstitial binding energy approaches 0 eV at 10–11 Angstroms. The mean difference in terms of the absorption length scale of GBs is on the order of 4 Angstroms, which is over a full lattice unit difference ($a_0=2.8553$ Angstroms) in terms of the affected length scale. A similar trend is observed for the maximum binding energies, i.e., the maximum binding energy approaches 0 eV at a greater distance for interstitials than for vacancies (not shown). This supports the finding that GBs tend to have a much larger length scale for absorption of interstitial atoms over vacancies as well.

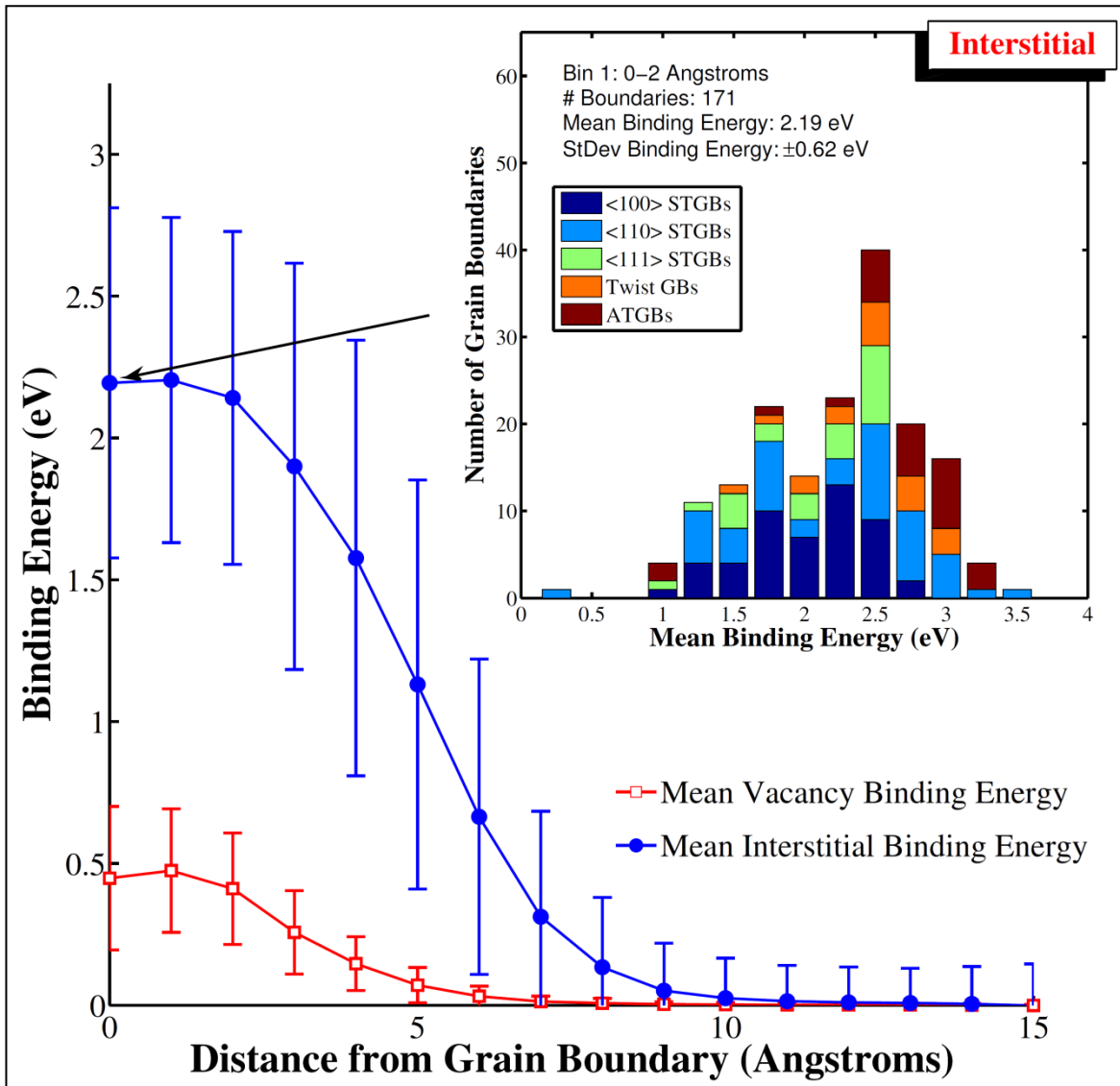


Figure 8. Evolution of the vacancy and interstitial mean binding energies as a function of the distance from the GB center.

Note: In figure 8 the mean binding energies for each 2 Angstroms bin are calculated from the binding energy distributions for the sampled GBs (inset histogram). GBs tend to have both a larger binding energy and absorption length scale for interstitial defects over vacancies.

How the GB character affects the energies and point defect absorption length scales was also investigated. Figure 9 shows how the mean vacancy and interstitial binding energies decrease as a function of distance for the different GB systems examined herein. This plot is similar to figure 9 with bins that are 2 Angstroms wide. First, in both plots, the <100> STGBs tend to have the lowest binding energy curves, while the asymmetric boundaries sampled tended to have the highest binding energy curves. The binding energy curves for the different systems tend to follow similar relationships with respect to distance from the GB center, with some curves

having slightly lower binding energies in the 0 Angstroms bin than bins a few Angstroms from the GB center. These results agree with those of Wen et al. (94), who used molecular dynamics to sample vacancy formation and diffusion energies in both $\Sigma 5$ STGBs for Fe and found that vacancies located within 8–10 layers from the GB center would tend to favorably migrate and aggregate to the second layer (i.e., just adjacent to the GB center). Again, the increase in mean binding energy for the 1 Angstroms bins in a few GB systems suggests that this behavior extends to more boundaries than just the $\Sigma 5$ sampled by Wen and colleagues. On another note, these plots show that the absorption length scale is affected by the GB character. While the mean vacancy binding energies approach 0 eV at very similar distances (~ 7 Angstroms), the mean interstitial binding energies approach 0 eV from 8 Angstroms ($\langle 100 \rangle$ STGBs) to 11 Angstroms (ATGBs). Clearly, both the mean point defect energies and the absorption length scale is affected by GB character. However, as Fig. 8 shows, the type of point defect is even more important in terms of characterizing the strength of the GB as a sink for point defects.

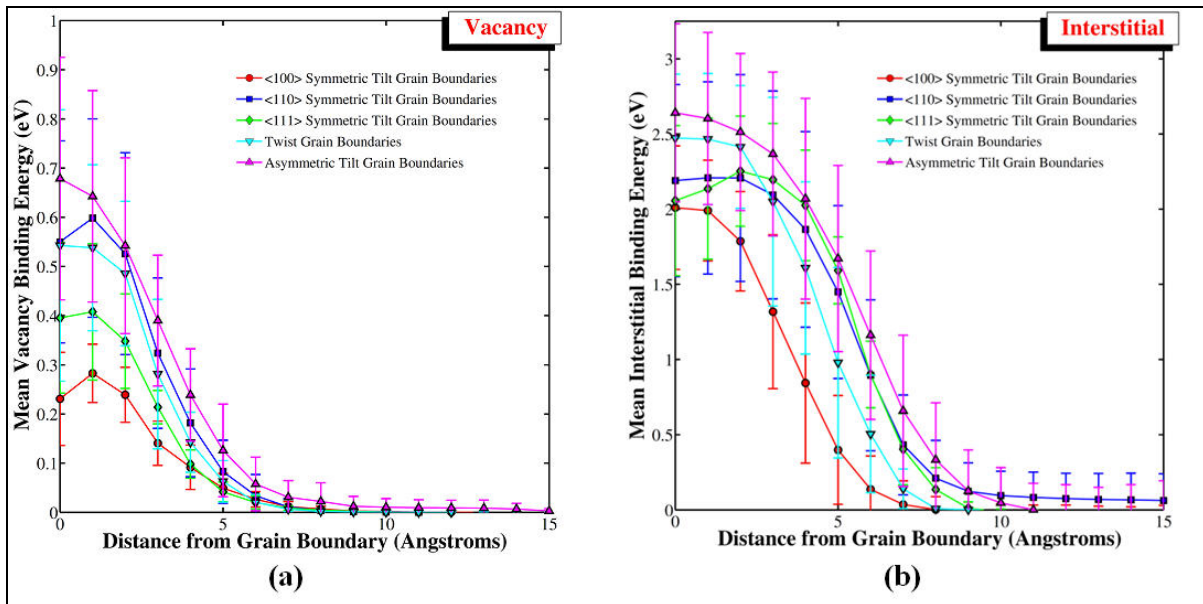


Figure 9. Evolution of the (a) vacancy and (b) interstitial mean binding energies as a function of the distance from the GB center.

Note: In figure 9 the mean binding energies for each 2 Angstroms bin are calculated from the binding energy distributions for the different GB systems displayed. The binding energy curves and absorption length scales for both interstitial defects and vacancies are sensitive to the type of GB system.

4.6 Extension to Fe-He system

This methodology can also be extended to the segregation of impurities and other elements to the GB, which can be important for GB embrittlement/strengthening, formation of second phases/precipitates at GBs, and radiation-induced segregation. The same methodology used for examining the interaction of point defects with the boundary has been applied to He. Multiple

different He defect species were examined in the present work: a single He atom in substitutional and interstitial sites, two He atoms in substitutional and interstitial sites, and multiple He atoms in a monovacancy. Multiple low- Σ GBs were chosen as well: four $\langle 100 \rangle$ STGBs and six $\langle 110 \rangle$ STGBs.

The evolution of the formation energy of three He defect types as a function of spatial position is shown in figure 10. In figure 10 (a), each atom is colored by the formation energy for a HeV defect. In figure 10 (b) and (c), each atom is colored by the formation energy for interstitial He nearby to an Fe atom. In these images, the color white is used to represent the bulk formation energy, for ease of locating atomic sites with formation energies that differ from the bulk. Also, note that the formation energies for interstitial He defects were obtained by using 20 different initial locations for each particular site. Therefore, if there are a number of local energy minima (e.g., octahedral sites versus tetrahedral sites), this technique will help with identifying the lowest formation energy for each site. Interestingly, as was previously found for point defects, there is a GB-affected region where the formation energies for the various He defect types are lower than in the bulk, thus providing a driving force for segregation to the boundary. Also, notice that for the interstitial He defect types, the $\Sigma 3(112)$ coherent twin has formation energies that are very similar to the bulk values, in contrast to the other boundaries studied. Moreover, this is not the case for the HeV defect, which has much lower formation energies near the $\Sigma 3(112)$ interface region. Last, the GBs are arranged in order of increasing misorientation angle. As the structure changes with increasing misorientation angle, it is observed that the mean formation energies of the various defect types change in a non-monotonic manner.

The formation energies for He₂ in the interstitial sites as a function of distance from the GB for six $\langle 110 \rangle$ STGBs is shown in figure 11. As with figure 10, for each site, twenty different interstitial starting positions centered around each Fe atom “site” were used. Formation energies within the GB region can be as much as 2.5 eV lower than those energies in the bulk, providing a strong driving force for He₂ to segregate to the boundaries. The gray region denotes the length scale of interaction with the He defect configuration, which is on the order of 4–5 Angstroms from the center of the GB. The edges of the GB affected region are defined as the distance that the formation energy is more than 5% lower than the bulk formation energy. The dotted lines in the figure correspond to increments of 5% of the bulk formation energy. Notice that the GB region can have up to 30% lower formation energies than in the bulk for He₂. These sorts of trends are also evident with the other He defect types as well.

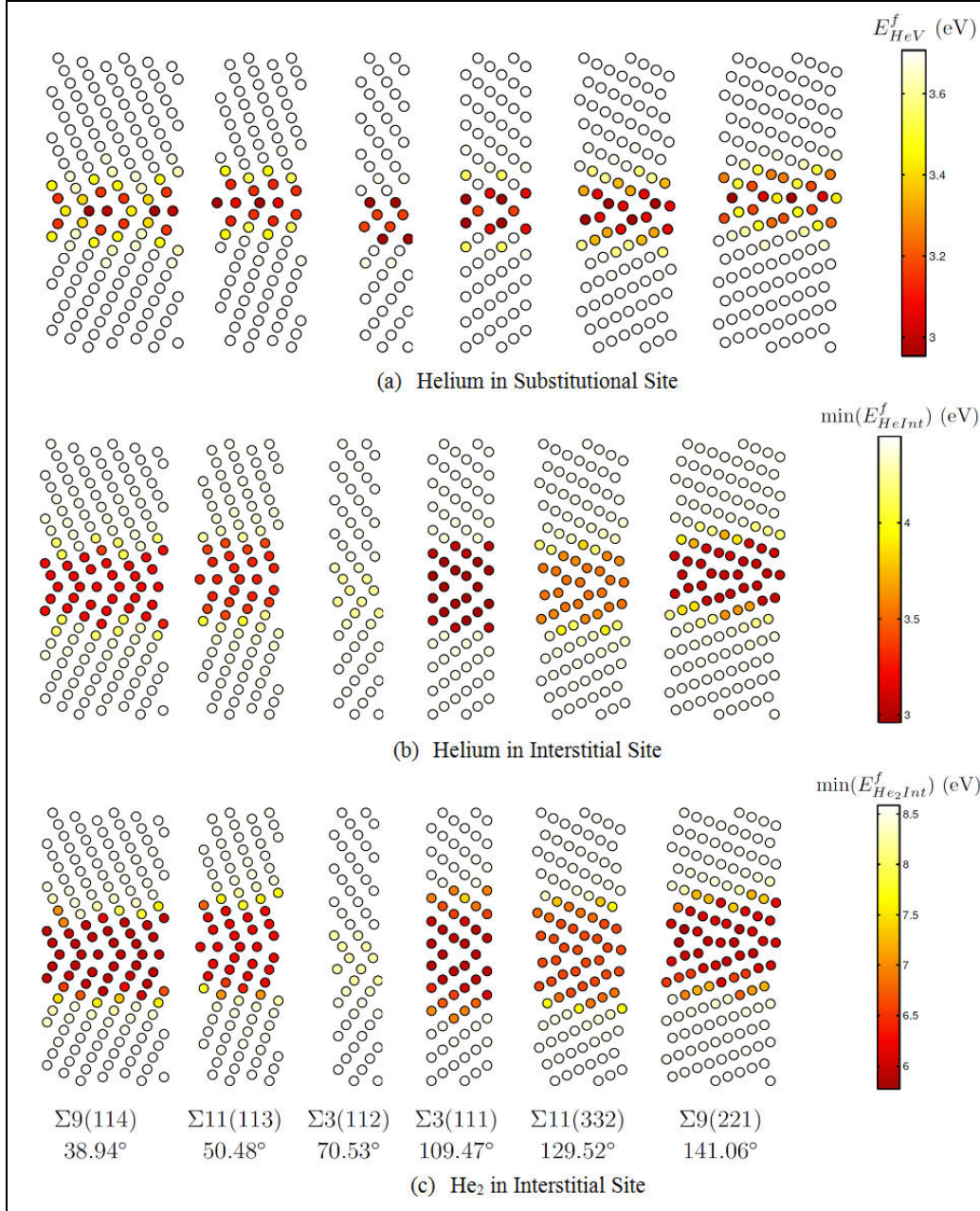


Figure 10. Formation energies of (a) He in substitutional sites, (b) He in interstitial sites, and (c) He₂ in interstitial sites as a function of spatial position for six $\langle 110 \rangle$ STGBs in order of increasing misorientation angle (left to right).

Note: Regarding figure 10, for He in the interstitial sites, twenty different interstitial starting positions centered around each Fe atom “site” were used; the minimum formation energies are shown.

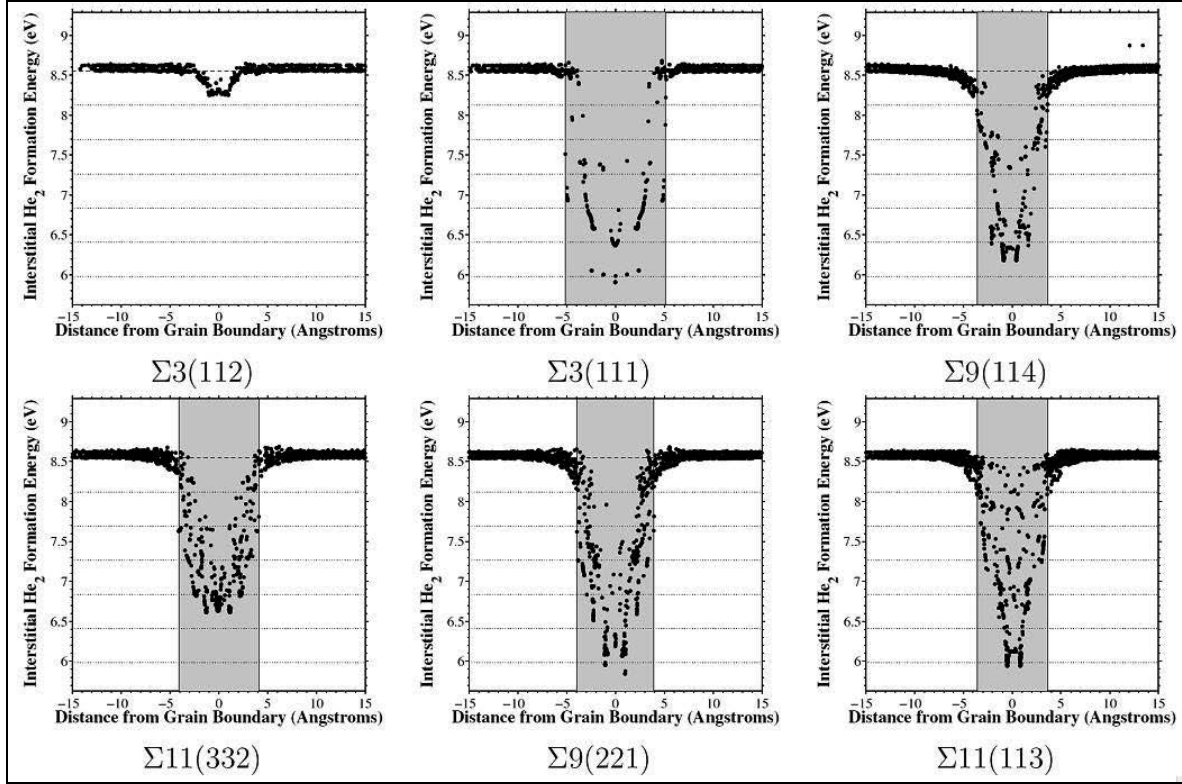


Figure 11. Formation energies for He_2 in the interstitial sites as a function of distance from the GB for six $\langle 110 \rangle$ STGBs.

Note: Regarding figure 11, for each site, twenty different interstitial starting positions centered around each Fe atom “site” were used. Formation energies within the GB region can be as much as 2.5 eV lower than those energies in the bulk, providing a strong driving force for He to segregate to the boundaries. The gray region denotes the length scale of interaction with the He defect configuration, which is on the order of 4–5 Angstroms from the center of the GB.

4.7 Extension to Fe-Cr system

This methodology has also been extended to investigating the segregation of Cr to the GB, an important by-product of radiation-induced segregation in some GBs within ferritic steels. As with He, multiple different Cr configurations were examined in the present work: a single Cr atom in a substitutional site, an Fe-Cr dumbbell configuration, two Cr atoms in a monovacancy, etc. Additionally, the formation energies and binding energies of CrV with both vacancies and CrV in first nearest neighbor sites were investigated. For this study, multiple low- Σ GBs were chosen: four $\langle 100 \rangle$ STGBs and six $\langle 110 \rangle$ STGBs.

The evolution of the formation energy of Cr_2V as a function of spatial position is shown in Figure 12. In figure 12, each atom is colored by the formation energy for Cr_2V configuration. In these images, the color white is again used to represent the bulk formation energy, for ease of locating atomic sites with formation energies that differ from the bulk. Also, note that the formation energies for Cr_2V were obtained using 20 different initial locations for each particular

site. Therefore, if there are a number of local energy minima (e.g., octahedral sites versus tetrahedral sites), this technique will help with identifying the lowest formation energy for each site. Thus, for each Cr configuration (and, more specifically, Cr₂V in figure 12), there are multiple formation energies associated with each site. Hence, the minimum (top), mean (middle), and standard deviation (bottom) were used to show the energies associated with each site. These images clearly show a GB-affected region where the formation energies for the Cr₂V configurations are lower than in the bulk. However, the bulk formation energies are on the order of 3 eV, which would tend to discourage this configuration from forming. In the GB region, though, the formation energies can actually be negative (shown in figure 12 by dark circles), providing an energetic driving force for Cr₂V to form. Also, notice that for the Cr₂V configurations, the Σ3(112) coherent twin again has formation energies that are very similar to the bulk values, in contrast to the other boundaries studied. By examining the standard deviation of the formation energies, it is observed that Cr₂V configurations close to the GB center tend to have a low formation energy no matter what the starting configuration. However, there is a transition region as the GB affected region transitions to the bulk crystalline region where the Cr₂V configurations can assume either a low or high formation energy depending on the orientation of the Cr₂, which may be important for the migration of this species.

The formation energies for Cr₂V configurations as a function of distance from the GB for four <100> STGBs is shown in figure 13. As with figure 12, for each site, twenty different Cr₂V starting positions centered around each monovacancy site were used. Formation energies within the GB region can be as much as 3 eV lower than those energies in the bulk, which may enable Cr₂V to form within the GB in certain scenarios. The gray region denotes the length scale of interaction with the Cr₂V defect configuration, which is on the order of >5 Angstroms from the center of the GB. The edges of the GB affected region are defined as the distance that the formation energy is more than 5% lower than the bulk formation energy. These sorts of trends are also evident with the other Cr defect types as well.

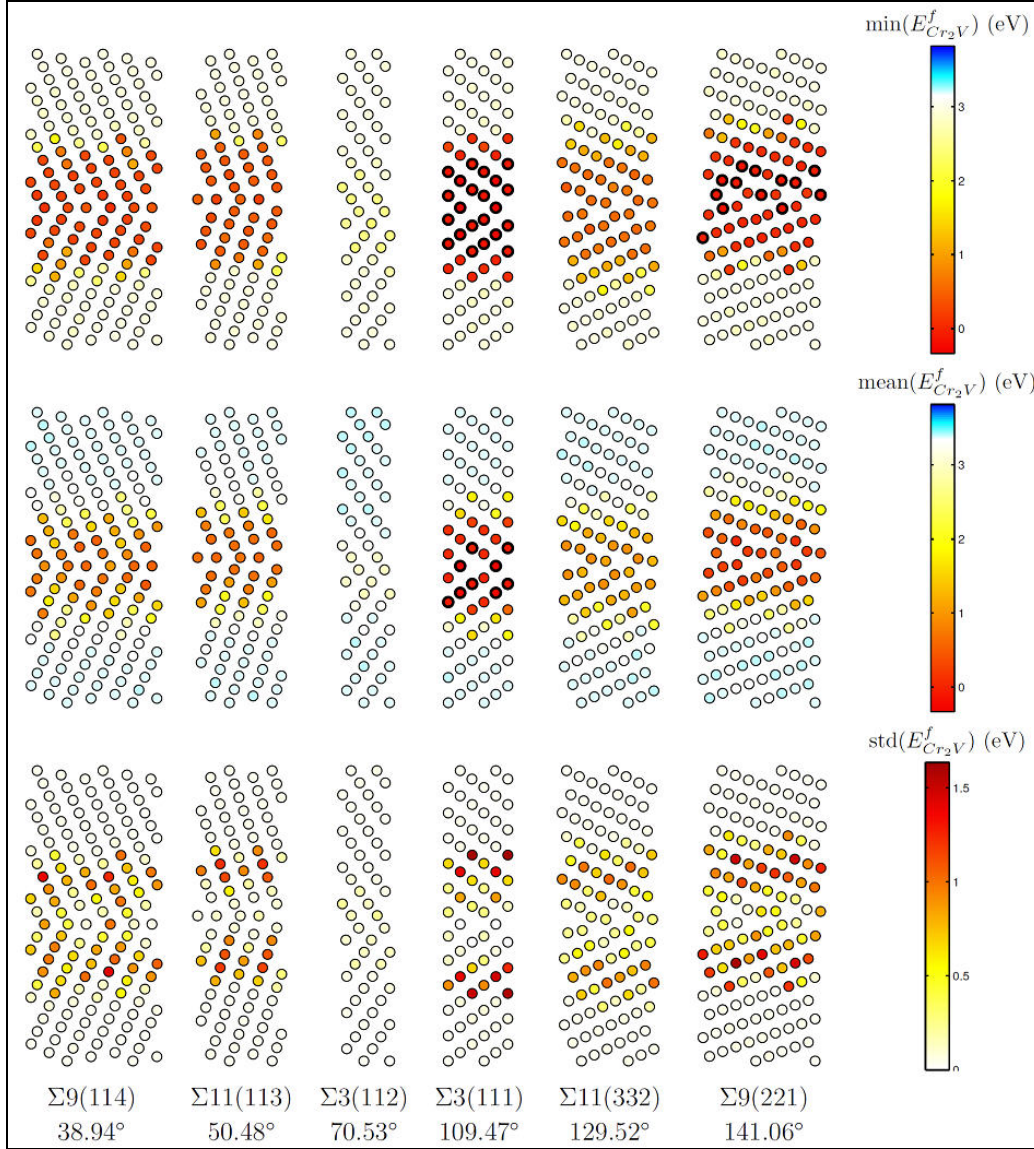


Figure 12. Formation energies of Cr_2V as a function of spatial position for six $\langle 110 \rangle$ STGBs in order of increasing misorientation angle (left to right).

Note: Regarding figure 12, for each monovacancy sites, twenty different Cr_2 starting positions centered around the site were used. These images show the minimum (top), mean (middle), and standard deviation (bottom) for the twenty formation energies at each site. Thick lines on the atom site represent that the formation energy is negative.

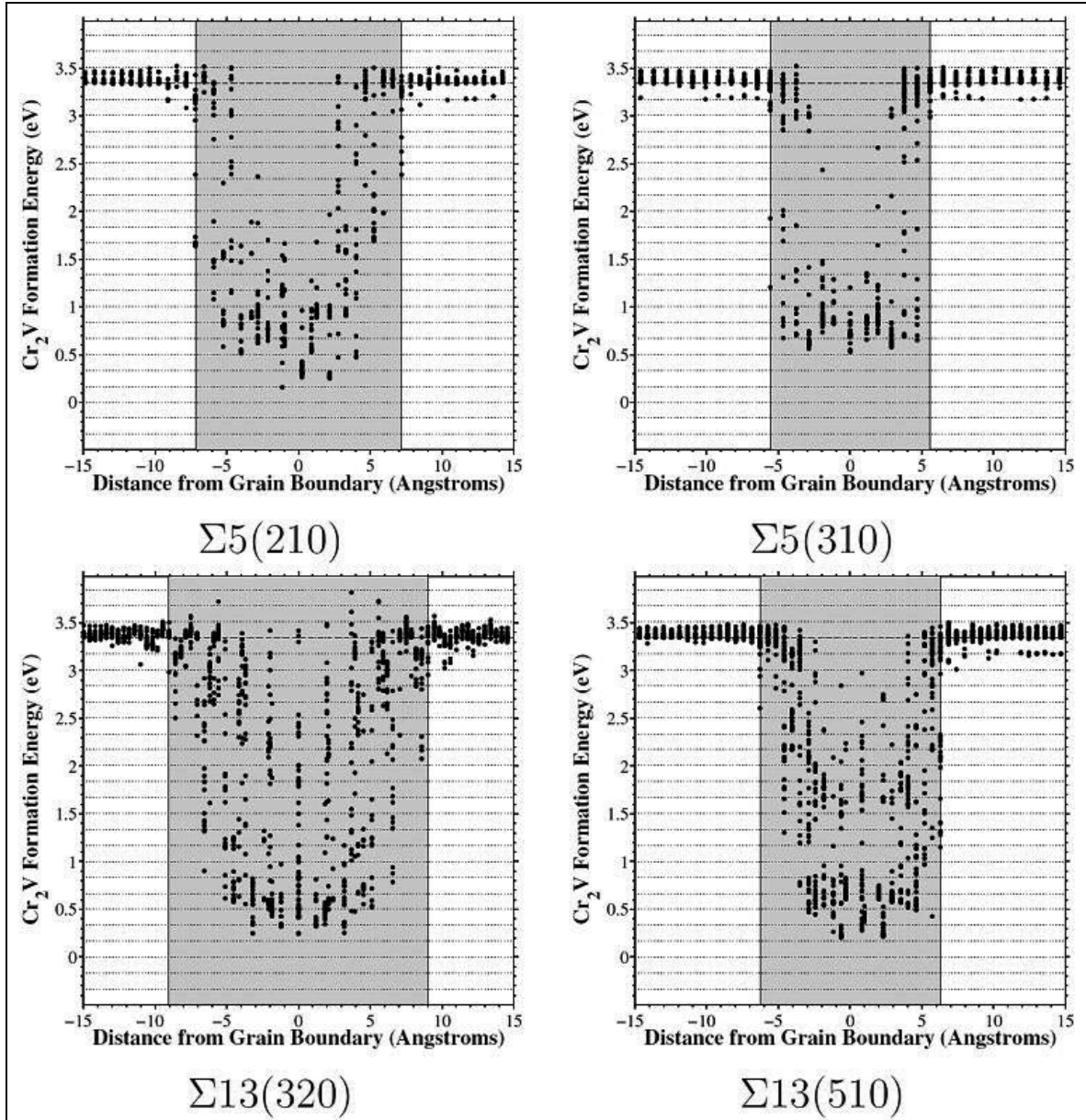


Figure 13. Formation energies for Cr_2V as a function of distance from the GB for four $\langle 100 \rangle$ STGBs.

Note: Regarding figure 13, for each site, twenty different interstitial starting positions centered around each Fe atom “site” were used. Formation energies within the GB region can approach 0 eV with some negative formation energies (for $\langle 110 \rangle$ boundaries, not shown). Again, the gray region denotes the length scale of interaction with the He defect configuration, which is on the order of >5 Angstroms from the center of the GB.

4.8 Framework for Interatomic Potential Development with Uncertainty Quantification

As an initial example, a framework for interatomic potential design (95, 96) was developed with an Fe-He interatomic potential design map and the modified embedded atom method (MEAM) (97) formulation to show its profound effect. MEAM has been reviewed many times before, and

more details are available in the literature (97–99). He interactions in Fe systems play an important role in the mechanical behavior of steel alloys. Molecular dynamics simulations with various potentials have shown that He and He cluster formation affects many physical properties in Fe (100–106). However, there has not been a comprehensive study to examine the limits of a single interatomic potential formulation for these observed behaviors. In this work, the generalized framework will generate an interatomic potential design map that can be used to explore and explain this nano-scale behavior.

The generalized framework is outlined in figure 14. While this framework is initially applied to Fe-He, this framework is not limited to development of Fe-He potentials and can be extended to develop single- and multiple-element interatomic potential design maps. The difficulty of fitting many-element potentials with traditional methods may be overcome by utilizing this framework. This framework is grouped into two stages: the Global Approach stage and Local Approach stage. The Global Approach is used as a coarse refinement of the interatomic potential, whereby the number of potential parameters and their ranges are reduced. The Local Approach then constructs the interatomic potential design maps—analytical models based on simulations that allow the user to tailor interatomic potentials for specific applications. This can be used to locally optimize the interatomic potential for the design space. The two stages have a number of steps, which will be briefly explained.

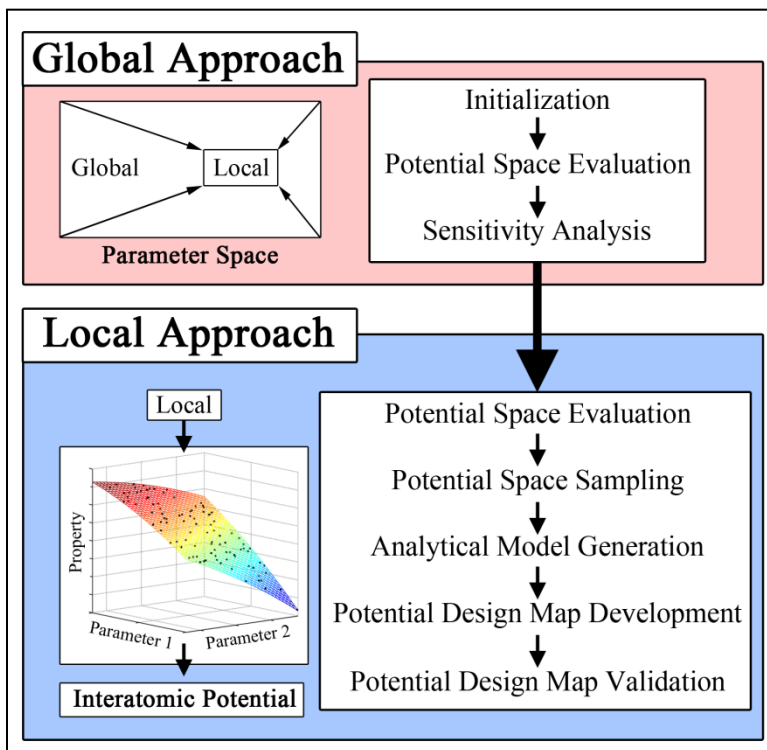


Figure 14. Schematic of the generalized framework for interatomic potential development showing the Global and Local Approach stages along with their individual steps.

Note: Regarding figure 14, the Global Approach is used as a coarse refinement of the interatomic potential, whereby the parameter space (number of potential parameters and their ranges) are reduced. The Local Approach then constructs the interatomic potential design maps—an analytical model based on simulations that allows the user to tailor interatomic potentials for specific applications.

To elucidate the relationship between these two parameters and the formation energies for the single He configurations, figure 15 (a) is an example plot showing the formation energies calculated by nano-scale simulations (black dots) for 100 Fe-He potentials while varying only the potential parameters, ρ_0^{He} and $\Delta H_{f,12}$. This plot shows the variation in formation energies to be smooth and nonlinear, with the correct formation energy ordering for low values of ρ_0^{He} and $\Delta H_{f,12}$. Only two parameters were selected for visualization purposes in figure 15 (a). However, in this work, a multi-dimensional space was used with five parameters and 2000 different potential parameter combinations for development of the Fe-He potential design map.

As an example of the interatomic potential design map, figure 15 (b) constructs a design map for the Fe-He system as a function of the five MEAM parameters used in the Local Approach stage. First, the MEAM parameters are normalized in all plots so that 0.5 represents the optimal MEAM potential parameter values and 0 (1) represents -2% ($+2\%$) of this value. Second, the formation energies are normalized by the *ab initio* values for the different configurations. Figure 15 (b) shows the effect of changing all five MEAM parameters on the He formation energies. The utility of such a design map is that it contains multiple potentials that can be formulated for specific properties. For instance, at a normalized parameter value of ~ 0.4 in figure 15 (b) the formation energies of He in the substitutional and tetrahedral interstitial sites are approximately equal to the *ab initio* values (i.e., $\sim 0\%$ normalized formation energies). If these two formation energies are critical to modeling nano-scale mechanisms, more so than the other properties in the design map, then perhaps this Fe-He interatomic potential would be the best potential for this particular application. On the other hand, if the formation energies of the stable $\langle 110 \rangle$ He₂V dumbbell and He₃V configuration are most important, then perhaps an Fe-He interatomic potential with slightly higher normalized parameter values (~ 0.6) would more accurately capture the associated nano-scale mechanisms. In this sense multiple potentials can be easily developed for different applications and the maps can be used to quantify the uncertainty in the potential development process, which may be important for understanding the accuracy of a multi-scale modeling framework that includes atomistic modeling with interatomic potentials.

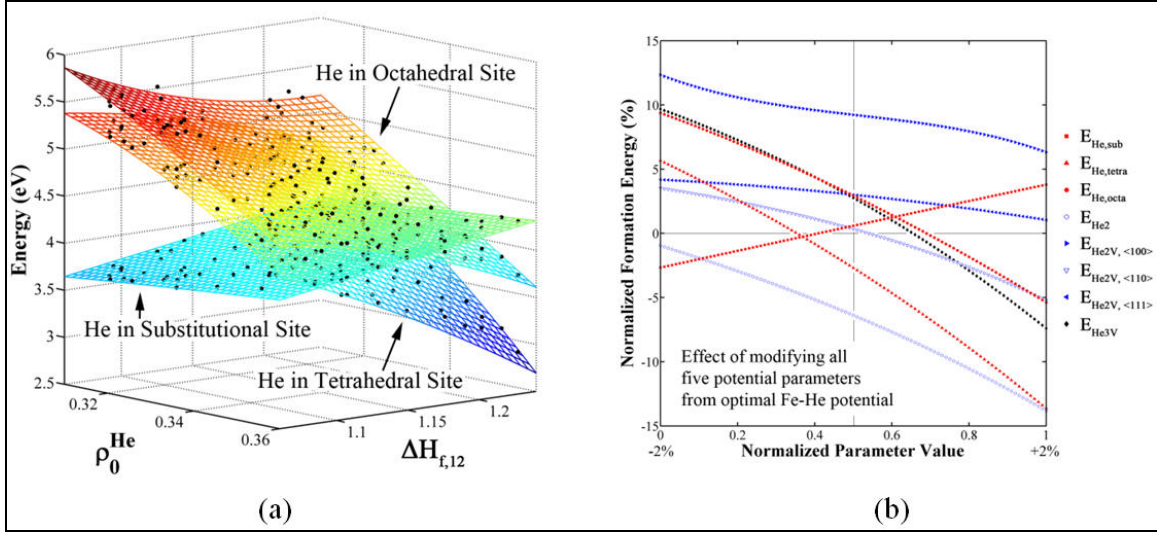


Figure 15. (a) Nanoscale calculations (black dots) and analytical surfaces for single He formation energies in the LA Potential Space Sampling and LA Analytical Model Generation step. Accurate development of analytical relationships between parameters and properties are critical for probing the interatomic potential design space. (b) Interatomic potential design map for the Fe-He system.

Note: Regarding figure 15, a change in the normalized parameter value from 0.5 reflects a deviation in all five MEAM parameters up to $\pm 2\%$. This cross-section through an n^{th} -dimensional design map shows how potentials can be tailored for specific properties.

5. Summary

We have investigated how GB structure influences the absorption of point defects and segregation of He and Cr for BCC Fe. Molecular statics simulations were used to generate a GB structure database that contained $\langle 100 \rangle$, $\langle 110 \rangle$ and $\langle 111 \rangle$ STGBs, twist GBs and ATGBs. Then, simulations were used to calculate formation and binding energies at all potential GB sites within 15 Angstroms of the boundary. The present results provide detailed information about the interaction energies of point defects and elements with GBs in Fe. In addition to providing detailed information about the interactions of various defect/element configurations with the local GB structure, these studies can provide energetic and length scale information that incorporates uncertainty due to the GB character to higher scale models. Moreover, a design optimization-based methodology was explored for interatomic potential development, whereby analytical meta-models of properties within a training database can be used to quantify uncertainty in the potential development process – a key step for quantifying the accuracy of multi-scale models that incorporate atomistic modeling results using interatomic potentials. Atomistic simulations of this nature can ultimately help our understanding of how interface

structure affects point defect and element segregation to GBs in polycrystalline materials and can improve the accuracy of multi-scale models by better understanding how information is passed to and from the nano-scale.

6. References

1. Was, G. S. *Fundamentals of Radiation Materials Science: Metals and Alloys*, 1st ed. (Springer, 2007).
2. Ackland, G. *Science*. **2010**, 327, 1587.
3. Allen, T. R.; Busby, J. T.; Was, G. S.; Kenik, E. A. *Journal of Nuclear Materials*. **1998**, 255, 44.
4. Bruemmer, S. M.; Simonen, E. P.; Scott, P. M.; Andresem, P. L.; Was, G. S.; Nelson, J. L. *Journal of Nuclear Materials*. **1999**, 274, 299.
5. Damcott, D. L.; Allen, T.; Was, G. S. *Journal of Nuclear Materials*. **1995**, 225, 97.
6. Duh, T. S.; Kai, J. J.; Chen, F. R.; Wang, L. H. *Journal of Nuclear Materials*. **1998**, 258–263, 2064.
7. Duh, T. S.; Kai, J. J.; Chen, F. R. *Journal of Nuclear Materials*. **2000**, 283–287, 198.
8. Duh, T. S.; Kai, J. J.; Chen, F. R.; Wang, L. H. *Journal of Nuclear Materials*. **2001**, 294, 267.
9. Etienne, A.; Radiguet, B.; Cunningham, N. J.; Odette, G. R.; Pareige, P. *Journal of Nuclear Materials*. **2010**, 406, 244.
10. Jiao, Z.; Was, G. S. *Acta Materialia*. **2011**, 59, 1220.
11. Lu, Z.; Faulkner, R. G.; Was, G.; Wirth, B. D. *Scripta Materialia*. **2008**, 58, 878.
12. Was, G. S.; Wharry, J. P.; Frisbie, B.; Wirth, B. D.; Morgan, D.; Tucker, J. D.; Allen, T. R. *Journal of Nuclear Materials*. **2011**, 411, 41.
13. Wharry, J. P.; Jiao, Z.; Shankar, V.; Busby, J. T.; Was, G. S. *Journal of Nuclear Materials*. **2011**, 417, 140.
14. Watanabe, S.; Takamatsu, Y.; Sakaguchi, N.; Takahashi, H. *Journal of Nuclear Materials*. **2000**, 283–287, 152.
15. Dollar, M.; Gleiter, H. *Scripta Metallurgica*. **1985**, 19, 481.
16. Watanabe, T. *Res Mechanica: International Journal of Structural Mechanics and Materials Science*. **1984**, 11, 47.

17. Rohrer, G. S.; Saylor, D. M.; Dasher, B. E.; Adams, B. L.; Rollett, A. D.; Wynblatt, P. *Zeitschrift fuer Metallkunde/Materials Research and Advanced Techniques*. **2004**, *95*, 197.
18. Rohrer, G. S.; Randle, V.; Kim, C.-S.; Hu, Y. *Acta Materialia*. **2006**, *54*, 4489.
19. Saylor, D. M.; Morawiec, A.; Rohrer, G. S. *Acta Materialia*. **2003**, *51*, 3663.
20. Saylor, D. M.; Dasher, B.S.E.; Rollett, A. D.; Rohrer, G. S. *Acta Materialia*. **2004**, *52*, 3649.
21. Kim, C.-S.; Hu, Y.; Rohrer, G. S.; Randle, V. *Scripta Materialia*. **2005**, *52*, 633.
22. Sekine, M.; Sakaguchi, N.; Endo, M.; Kinoshita, H.; Watanabe, S.; Kokawa, H.; Yamashita, S.; Yano, Y.; Kawai, M. *Journal of Nuclear Materials*. **2011**, *414*, 232.
23. Bai, X.; Voter, A. F.; Hoagland, R. G.; Nastasi, M.; Uberuaga, B. P. *Science*. **2010**, *327*, 1631.
24. Samaras, M.; Derlet, P. M.; Van Swygenhoven, H.; Victoria, M. *Journal of Nuclear Materials*. **2006**, *351*, 47.
25. Samaras, M.; Derlet, P. M., Van Swygenhoven, H.; Victoria, M. *Nuclear Instruments and Methods in Physics Research Section B: Beam Interactions with Materials and Atoms*. **2003**, *202*, 51.
26. Samaras, M.; Derlet, P. M.; Van Swygenhoven, H.; Victoria, M. *Journal of Nuclear Materials*. **2003**, *323*, 213.
27. Samars, M.; Derlet, P. M.; Van Swygenhoven, H.; Victoria, M. *Philosophical Magazine*. **2003**, *83*, 3599.
28. Millett, P. C.; Wolf, D.; Desai, T.; Yamakov, V. *Applied Physics Letters*. **2008**.
29. Millett, P. C.; Aidhy, D. S.; Desai, T.; Phillpot, S. R.; Wolf, D. *International Journal of Materials Research*. **2009**, *100*, 550.
30. Gao, N.; Samaras, M.; Van Swygenhoven, H. *Journal of Nuclear Materials*. **2010**, *400*, 240.
31. Perez-Perez, F. J.; Smith, R. *Nuclear Instruments and Methods in Physics Research Section B: Beam Interactions with Materials and Atoms*. **1999**, *153*, 136.
32. Perez-Perez, F. J.; Smith R. *Nuclear Instruments and Methods in Physics Research Section B: Beam Interactions with Materials and Atoms*. **2001**, *180*, 322.
33. Misra, A.; Demkowicz, M. J.; Wang, J.; Hoagland, R. G. *JOM*. **2008**, *60*, 39.
34. Misra, A.; Demkowicz, M. J.; Zhang, X.; Hoagland, R. G. *JOM*. **2007**, *59*, 62.
35. Heinisch, H. L.; Gao, F.; Kurtz, R. J. *Journal of Nuclear Materials*. **2004**, *329–333*, 924.

36. Kwok, T.; Ho, P. S.; Yip, S.; Balluffi, R. W.; Bristowe, P. D.; Brokman, A. *Physical Review Letters* **1981**, *47*, 1148.
37. Kwok, T.; Ho, P. S.; Yip, S. *Physical Review B* **29**, **1984**, 5354.
38. Kwok, T.; Ho, P. S.; Yip, S. *Physical Review B* **29**, **1984**, 5363.
39. Suzuki, A.; Mishin, Y. *Interface Science*. **2003**, *11*, 131.
40. Suzuki, A.; Mishin, Y. *Journal of Materials Science*. **2005**, *40*, 3155.
41. Suzuki, A.; Mishin, Y. *Interface Science*. **2003**, *11*, 425.
42. Demkowicz, M. J.; Anderoglu, O.; Zhang, X.; Misra, A. *Journal of Materials Research*. **2011**, *26*, 1666.
43. Forwood, C.; Clarebrough, L. *Electron microscopy of interfaces in metals and alloys* (IOP Publishing Ltd, 1991).
44. Forwood, C. T.; Clarebrough L. M. *Philosophical Magazine A*. **1986**, *53*, 863.
45. Duparc, O. H.; Poulat, S.; Larere, A.; Thibault, J.; Priester, L. *Philosophical Magazine A*. **2000**, *80*, 853.
46. Duparc, O. H.; Couzinie, J.-P.; Thibault-Penisson, J.; Lartigue-Korinek, S.; Decamps, B.; Priester, L. *Acta Materialia*. **2007**, *55*, 1791.
47. Sutton, A. P.; Balluffi, R. W. *Interfaces in Crystalline Materials* (Oxford University Press, USA, 1997).
48. Wolf, D.; Yip, S. *Materials Interfaces: Atomic-level Structure and Properties*, 1st ed. (Springer, 1992).
49. Sutton, A. P.; Vitek, V. *Philosophical Transactions of the Royal Society of London. Series A. Mathematical and Physical Sciences*. **1983**, *309*, 1.
50. Sutton, A. P.; Vitek, V. *Philosophical Transactions of the Royal Society of London. Series A. Mathematical and Physical Sciences*. **1983**, *309*, 37.
51. Sutton, A. P.; Vitek, V. *Philosophical Transactions of the Royal Society of London. Series A. Mathematical and Physical Sciences*. **1983**, *309*, 55.
52. Wang, G.-J.; Vitek, V. *Acta Metallurgica* **1986**, *34*, 951.
53. Vitek, V.; Sutton, A. P.; Wang, G. J.; Schwartz, D. *Scripta Metallurgica*. **1983**, *17*, 183.
54. Wang, G. J.; Sutton, A. P.; Vitek, V. *Acta Metallurgica*. **1984**, *32*, 1093.
55. Vitek, V.; Minonishi, Y.; Wang, G. J. *Journal de Physique*. **1985**, *46*, C4.

56. The importance of which was demonstrated in Wolf, D. *Scripta Metallurgica*. **1989**, 23, 1713.
57. Wolf, D. *Scripta Metallurgica*. **1989**, 23, 1913.
58. Wolf, D. *Acta Metallurgica et Materialia*. **1990**, 38, 791.
59. Wolf, D. *Acta Metallurgica et Materialia*. **1990**, 38, 781.
60. Holm, E. A.; Olmsted, D. L.; Foiles, S. M. *Scripta Materialia*. **2010**, 63, 905.
61. Tschopp, M. A.; Tucker, G. J.; McDowell, D. L. *Acta Materialia*. **2007**, 55, 3959.
62. Tschopp, M. A.; Spearot, D. E.; McDowell, D. L. *Modelling and Simulation in Materials Science and Engineering*. **2007**, 15, 693.
63. Tschopp, M. A.; McDowell, D. L. *Philosophical Magazine*. **2007**, 87, 3871.
64. Tschopp, M. A.; McDowell, D. L. *Philosophical Magazine*. **2007**, 87, 3147.
65. Tschopp, M. A.; McDowell, D. L. *Journal of Materials Science*. **2007**, 42, 7806.
66. Olmsted, D. L.; Holm, E.; Foiles, S. *Acta Materialia*. **2009**, 57, 3704.
67. Olmsted, D. L.; Foiles, S.; Holm, E. *Acta Materialia*. **2009**, 57, 3694.
68. Spearot, D. E.; Jacob, K. I.; McDowell, D. L. *Acta Materialia*. **2005**, 53, 3579.
69. Spearot, D. E.; Tschopp, M. A.; Jacob, K. I.; McDowell, D. L. *Acta Materialia*. **2007**, 55, 705.
70. Spearot, D. E.; Tschopp, M. A.; McDowell, D. L. *Scripta Materialia*. **2009**, 60, 675.
71. Tschopp, M. A.; Spearot, D. E.; McDowell, D. L. Chapter 82 Influence of Grain Boundary Structure on Dislocation Nucleation in FCC Metals, Vol. 14 (2008).
72. Tschopp, M. A.; Tucker, G. J.; McDowell, D. L. *Computational Materials Science*. **2008**, 44, 351.
73. Tschopp, M. A.; McDowell, D. L. *Scripta Materialia*. **2008**, 58, 299.
74. Tschopp, M. A.; McDowell, D. L. *International Journal of Plasticity*. **2008**, 24, 191.
75. Tucker, G. J.; Tschopp, M. A.; McDowell, D. L. *Acta Materialia*. **2010**, 58, 6464.
76. Dewald, M. P.; Curtin, W. A. *Modelling and Simulation in Materials Science and Engineering*. **2007**, 15, S193.
77. Dewald, M. P.; Curtin, W. A. *Philosophical Magazine*. **2007**, 87, 4615.

78. Dewald, M. P.; Curtin, W. A. *Modelling and Simulation in Materials Science and Engineering*. **2011**, 19.
79. Tschopp, M. A.; Horstemeyer, M. F.; Gao, F.; Sun, X.; Khaleel, M. *Scripta Materialia*. **2011**, 64, 908.
80. Plimpton, S. *Journal of Computational Physics*. **1995**, 117, 1.
81. Rittner, J. D.; Seidman, D. N.; Merkle, K. L. *Physical Review B* **1996**, 53, R4241.
82. Mendeleev, M. I.; Han, S.; Srolovitz, D. J.; Ackland, G. J.; Sun, D. Y.; Asta, M. *Philosophical Magazine* **2003**, 83, 3977.
83. NIST Interatomic Potential Website, <http://www.ctcms.nist.gov/potentials/index.html>, accessed 11/20/12.
84. Daw, M. S.; Baskes, M. I. *Physical Review B*. **1984**, 29, 6443.
85. Daw, M. S.; Baskes, M. I. *Physical Review Letters*. **1983**, 50, 1285.
86. Malerba, L.; Marinica, M. C.; Anento, N.; Bjrkas, C.; Nguyen, H.; Domain, C.; Djurabekova, F.; Olsson, P.; Nordlund, K.; Serra, A.; Terentyev, D.; Willaime, F.; Becquart, C. S. *Journal of Nuclear Materials*. **2010**, 406, 19.
87. Rittner, J. D.; Seidman, D. N. *Physical Review B*. **1996**, 54, 6999.
88. Bishop, G. H., Chalmers B. *Scripta Metallurgica*. **1968**, 2, 133.
89. Bishop, G. H.; Chalmers, B. *Philosophical Magazine*. **1971**, 24, 515.
90. Sutton, A. P. *Philosophical Magazine*. **1989**, 59, 53.
91. Read, W. T., Shockley, W. *Physical Review*. **1950**, 78, 275.
92. Humphreys, F.; Hatherly, M. Recrystallization and related annealing phenomena (Pergamon, 1995).
93. Tschopp, M. A.; Solanki, K.N.; Gao, F.; Sun, X.; Khaleel, M.; Horstemeyer, M. *Physical Review B*. **2012**, 85, 064108.
94. Wen, Y.-N.; Zhang, Y.; Zhang, J.-M.; Xu, K.-W. *Computational Materials Science*, **2011**, 50, 2087.
95. Tschopp, M. A.; Solanki, K.; Baskes, M.; Gao, F.; Sun, X.; Horstemeyer, M. *Journal of Nuclear Materials*, 425(1-3), 22–32.

96. Tschopp, M.; Solanki, K.; Horstemeyer, M. Tools developed and needed to realize the vision of integrated computational materials engineering, (ASM International, 2011) Chap. A Generalized Framework for Quantifying Material Structure-Property Relationships and Uncertainties: Applicability to ICME.
97. Baskes, M. I. *Physical Review B*. **1992**, *46*, (5), 2727.
98. Baskes, M.; Nelson, J.; Wright, A. *Physical Review B*. **1989**, *40*, 6085–6100.
99. Baskes, M.; Johnson, R. *Modelling and Simulation in Materials Science and Engineering*. **1994**, *2*, 147–163.
100. Morishita, K.; Sugano, R.; Wirth, B. D. *Journal of Nuclear Materials*. Dec. 2003, 323, 243–250.
101. Gao, F.; Heinisch, H.; Kurtz, R. *Journal of Nuclear Materials*. **2006**, *351*, 133–140.
102. Gao, F.; Heinisch, H.; Kurtz, R. *Journal of Nuclear Materials*. **2009**, 386–388 (C), 390–394.
103. Heinisch, H.; Gao, F.; Kurtz, R.; Le, E. *Journal of Nuclear Materials*. **2006**, *351* (1–3), 141–148.
104. Heinisch, H.; Gao, F.; Kurtz, R. *Journal of Nuclear Materials*. **2007**, 367–370, 311–315.
105. Terentyev, D.; Juslin, N.; Nordlund, K.; Sandberg, N. *Journal of Applied Physics*. **2009**, *105* (10), 103509.
106. Terentyev, D.; He, X. *Computational Materials Science*. **2010**, *49* (10), 858–864.

List of Symbols, Abbreviations, and Acronyms

2D	two-dimensional
3D	three-dimensional
ATGB(s)	asymmetric tilt grain boundary(ies)
BCC	body-centered cubic
CSL	coincident site lattice
DFT	Density Functional Theory
eV	electron volt
FCC	face-centered cubic
Fe-Cr	iron-chromium
GB(s)	grain boundary(ies)
He	helium
LAMMP_S	Large-scale Atomic/Molecular Massively Parallel Simulator
MD	molecular dynamics
MEAM	modified embedded atom method
NEAMS	Nuclear Energy Advanced Modeling and Simulation
PNNL	Pacific Northwest National Laboratory
SIA(s)	self-interstitial atom(s)
STGB(s)	symmetric tilt grain boundary(ies)

NO. OF
COPIES ORGANIZATION

1 DEFENSE TECHNICAL
(PDF INFORMATION CTR
only) DTIC OCA
8725 JOHN J KINGMAN RD
STE 0944
FORT BELVOIR VA 22060-6218

1 DIRECTOR
US ARMY RESEARCH LAB
IMAL HRA
MAIL & RECORDS MGMT
2800 POWDER MILL RD
ADELPHI MD 20783-1197

1 DIRECTOR
US ARMY RESEARCH LAB
RDRL CIO LL
2800 POWDER MILL RD
ADELPHI MD 20783-1197

1 DIRECTOR
US ARMY RESEARCH LAB
RDRL CIO LT
2800 POWDER MILL RD
ADELPHI MD 20783-1197

ABERDEEN PROVING GROUND

2 DIR USARL
RDRL WMM F
M TSCHOPP (1 HC, 1 CD)

INTENTIONALLY LEFT BLANK.